Central Washington University

ScholarWorks@CWU

The Crust and Upper Mantle Structure of Central and West Antarctica From Bayesian Inversion of Rayleigh Wave and Receiver Functions

Weisen Shen
Washington University in St. Louis

Audrey D. Huerta
Central Washington University

J. Paul Winberry
Central Washington University

Recommended Citation

Shen, W., Wiens, D. A., Anandakrishnan, S., Aster, R. C., Gerstoft, P., Bromirski, P. D., et al. (2018). The crust and upper mantle structure of central and West Antarctica from Bayesian inversion of Rayleigh wave and receiver functions. Journal of Geophysical Research: Solid Earth, 123, 7824–7849. https://doi.org/10.1029/2017JB015346

RESEARCH ARTICLE

Key Points:
- We present a new 3-D crustal and uppermost mantle model for central and West Antarctica based on 15 years of seismic data
- Surface waves from ambient noise and earthquakes and receiver functions are combined to improve the resolution
- New features such as an uppermost mantle anomaly beneath the Gamburtsev Mountains are discussed

Supporting Information:
- Supporting Information S1

Correspondence to:
W. Shen,
weisen.shen@stonybrook.edu

The Crust and Upper Mantle Structure of Central and West Antarctica From Bayesian Inversion of Rayleigh Wave and Receiver Functions

Weisen Shen[1,2] (ID), Douglas A. Wiens[1] (ID), Sridhar Anandakrishnan[3] (ID), Richard C. Aster[4] (ID), Peter Gerstoft[5] (ID), Peter D. Bromirski[5] (ID), Samantha E. Hansen[6], Ian W. D. Dalziel[7], David S. Heeszel[8], Audrey D. Huerta[9], Andrew A. Nyblade[3] (ID), Ralph Stephen[10], Terry J. Wilson[11], and J. Paul Winberry[9]

[1]Department of Earth and Planetary Sciences, Washington University, St. Louis, MO, USA, [2]Department of Geosciences, Stony Brook University - State University of New York, Stony Brook, NY, USA, [3]Department of Geosciences, Penn State University, University Park, PA, USA, [4]Department of Geosciences and Warner College of Natural Resources, Colorado State University, Fort Collins, CO, USA, [5]Scripps Institution of Oceanography, University of California, San Diego, CA, USA, [6]Department of Geological Sciences, University of Alabama, Tuscaloosa, AL, USA, [7]Institute for Geophysics, Jackson School of Geosciences, University of Texas at Austin, Austin, TX, USA, [8]U.S. Nuclear Regulatory Commission, Washington, DC, USA, [9]Department of Geological Sciences, Central Washington University, Ellensburg, WA, USA, [10]Woods Hole Oceanographic Institution, Woods Hole, MA, USA, [11]Department of Geological Sciences, Ohio State University, Columbus, OH, USA

Abstract We construct a new seismic model for central and West Antarctica by jointly inverting Rayleigh wave phase and group velocities along with P wave receiver functions. Ambient noise tomography exploiting data from more than 200 seismic stations deployed over the past 18 years is used to construct Rayleigh wave phase and group velocity dispersion maps. Comparison between the ambient noise phase velocity maps with those constructed using teleseismic earthquakes confirms the accuracy of both results. These maps, together with P receiver function waveforms, are used to construct a new 3-D shear velocity (Vs) model for the crust and uppermost mantle using a Bayesian Monte Carlo algorithm. The new 3-D seismic model shows the dichotomy of the tectonically active West Antarctica (WANT) and the stable and ancient East Antarctica (EANT). In WANT, the model exhibits a slow uppermost mantle along the Transantarctic Mountains (TAMs) front, interpreted as the thermal effect from Cenozoic rifting. Beneath the southern TAMs, the slow uppermost mantle extends horizontally beneath the traditionally recognized EANT, hypothesized to be associated with lithospheric delamination. Thin crust and lithosphere observed along the Amundsen Sea coast and extending into the interior suggest involvement of these areas in Cenozoic rifting. EANT, with its relatively thick and cold crust and lithosphere marked by high Vs, displays a slower Vs anomaly beneath the Gamburtsev Subglacial Mountains in the uppermost mantle, which we hypothesize may be the signature of a compositionally anomalous body, perhaps remnant from a continental collision.

1. Introduction

Knowledge of the basic attributes of the lithosphere, such as its seismic properties, Moho depths, lithosphere thickness, temperature, and composition, plays an important role in understanding the tectonic history of the continents. Obtaining such knowledge about continental Antarctica is especially important because limited information can be retrieved from geologic exposures, as approximately 99% of the continent is ice-covered. It is also important to understand the interaction between the Antarctic lithosphere (and the deeper mantle) with the ice sheet, as its thermal state contributes to the change of the thick ice sheet in a warming Earth. For instance, the thickness and temperature of the West Antarctic lithosphere impact the surface heat flow, which provides important boundary conditions to model the ice sheet dynamics (e.g., Blankenship et al., 1993; Fahnestock et al., 2001; Pollard et al., 2005). Additionally, knowing the seismic structure also helps to constrain the strength and viscosity of the lithosphere and mantle, which are essential for understanding glacial isostatic adjustment (GIA; e.g., van der Wal et al., 2015), and are important for modeling the projected evolution and stability of ice sheets into the future (e.g., Gomez et al., 2015). Thus, better constraints on lithospheric structure are needed to improve our knowledge of the interaction between tectonics, the cryosphere, and Earth's climate (Morelli & Danesi, 2004).

Before the last decade, most seismic investigations of Antarctica were focused on controlled source experiments that provide localized images and constraints (e.g., Ikami & Ito, 1986; Kogan, 1972; Stern & ten Brink, 1989) and passive source investigations that generated low resolution images at larger scales (e.g., surface wave studies by Bannister et al., 2000; Rouland & Roult, 1992; Ritzwoller et al. (2001); Danesi and Morelli (2000, 2001), Sieminski et al., 2003; Morelli & Danesi, 2004). These studies had highly limited resolution due to a lack of seismic stations deployed in remote Antarctica but clearly revealed first-order structure across the continent. Most fundamentally, these early studies all revealed a strong dichotomy in lithospheric structure: West Antarctica (WANT) is underlain by thin crust and thin, seismically slow lithosphere whereas East Antarctica (EANT) is underlain by thicker crust and thick, seismically fast lithosphere.

Since 2001, regional seismic experiments such as TAMSEIS (2001–2003), AGAP/GAMSEIS (2007–2009), ANET/POLENET (2008-present), RIS/DRIS (2014–2016), and TAMNNET (2012–2015) have accumulated a tremendous amount of seismic data that have enabled new, higher-resolution investigations of Antarctic crust and mantle structure. Studies have included body wave tomography (Brenn et al., 2017; Hansen et al., 2014; Lloyd et al., 2013, 2015; Watson et al., 2006), teleseismic surface waves (An et al., 2015; Graw et al., 2016; Heeszel et al., 2013, 2016; Lawrence et al., 2006a; Vuan et al., 2005), surface waves derived from ambient noise (Pyle et al., 2010), receiver functions (Chaput et al., 2014; Emry et al., 2015; Finotello et al., 2011; Hansen et al., 2009, 2010, 2016; Ramirez et al., 2016, 2017), seismic attenuation (Lawrence et al., 2006b), and shear wave splitting (Accardo et al., 2014; Barklage et al., 2009; Graw & Hansen, 2017). These studies have revealed a number of new details of lithospheric structure, especially at regional scales.

In this study, we construct a 3-D model at a continental scale by incorporating data from all available seismic arrays and by analyzing them with the recently developed data processing and imaging techniques. These techniques include ambient noise tomography (Sabra et al., 2005; Shapiro et al., 2005) that utilizes short-period surface waves and provides better constraints of the crustal structure, and Monte Carlo inversion of multiple seismic data sets (Shen, Ritzwoller, Schulte-Pelkum, & Lin, 2013), which provides quantitative assessment of the tomographic results and uncertainties. These tools have recently resulted in several large-scale high-resolution 3-D crustal and uppermost mantle models for other continents, such as the continental United States (Shen, Ritzwoller, & Schulte-Pelkum, 2013; Shen & Ritzwoller, 2016, and eastern Asia (Kang et al., 2016)). The resulting shear wave structure map covers the areas of Antarctica that have been well sampled with seismic instrumentation, including most of central and WANT.

In this paper, we first introduce the tectonic setting of continental Antarctica and then describe the seismic data sets used in this study. They include (1) short-period Rayleigh wave phase and group velocity maps derived from ambient noise tomography (ANT), (2) long-period phase velocity maps using teleseismic earthquakes compiled by Heeszel et al. (2016), and (3) *P* receiver functions (PRFs) used to further constrain abrupt interfaces at places where stations are deployed. The different seismic data sets are jointly implemented via a Bayesian Monte Carlo sampling algorithm and, at each local site, a posterior distribution is generated. Although all three data sets are well explained by a simple model parameterization for most of the stations, the Moho depth is not as precisely determined as for other continents when PRFs are incorporated (e.g., North America by Shen and Ritzwoller, 2016), because most PRFs from Antarctica are contaminated by body wave reverberations due to the thick ice sheet (e.g., Chaput et al., 2014). However, we show in this paper that these reverberations do not prevent identification of important structural features. After presenting images of the 3-D model, we discuss the uppermost mantle features that are either wholly new or have been poorly resolved in previous studies using more limited data sets. In the last section, we also describe some possible future work motivated by the findings of this study.

2. Tectonic Setting of the Study Region

Antarctica can be divided into two major regions (Figure 1b): WANT where the Mesozoic to Cenozoic West Antarctic Rift System (WARS), with associated volcanism, dominates its recent tectonics (Behrendt et al., 1991), and EANT, which is regarded as a Proterozoic craton which was once at the core of the Gondwana supercontinent (Boger, 2011; Du Toit, 1937; Fitzsimons, 2000a, 2000b; Veevers, 2012). In WANT, Marie Byrd Land (MBL) is a prominent region of uplift, accompanied by extensive Cenozoic sub ice and subaerial volcanism (LeMasurier, 1990; Wörner, 1999). Geochemically, its magmas indicate the signature of a possible deep mantle source (Panter et al., 1997; Weaver et al., 1994; Wörner, 1999) yet a high-temperature conduit
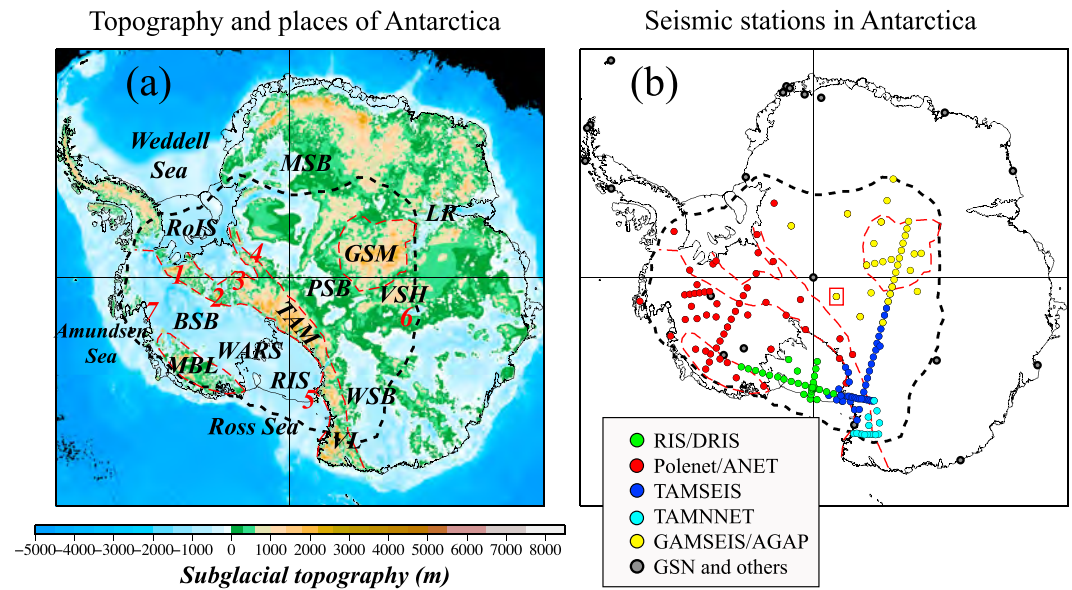
Topography and places of Antarctica

Seismic stations in Antarctica

Figure 1. Subglacial bedrock topography and seismic station coverage of Antarctica. (a) Key geographic features are marked on top of the subglacial bedrock topography (Fretwell et al., 2013). Abbreviations of geographic features mentioned in the paper are marked: BSB, Byrd Subglacial Basin; GSM, Gamburtsev Subglacial Mountains; LR,: Lambert Rift; MBL, Marie Byrd Land; MSB, Maud Subglacial Basin; PSB,: Polar Subglacial Basin; RIS, Ross Ice Shelf; RoIS, Ronne Ice Shelf; TAMs, Transantarctic Mountains; WSB, Wilkes Subglacial Basin; VL, Victoria Land; WARS, West Antarctic Rift System; VSH, Vostok Subglacial Highland. The WARS refers to the areas including both BSB and RIS. Locations of smaller-scale features are marked by numbers. 1, Ellsworth Mountains; 2, Whitmore Mountains; 3, Thiel Mountains; 4, Pensacola Mountains; 5, Ross Island; 6, Vostok Subglacial Lake; 7, Amundsen Sea Embayment (ASE). The black dashed line outlines the study area, defined by the surface wave map coverage. The red dashed contours outline high-elevation areas beneath the EM-WM-TM-TAMs, MBL, and GSM. (b) Seismic station locations, marked by circles where their color indicates their corresponding network. Contours are the same as in (a). A small red box marks the site of POLENET station SWEI.

extending into the deep mantle has not been definitely established (Emry et al., 2015; Hansen et al., 2014). The relationship between the WARS and MBL uplift is unclear (Behrendt & Cooper, 1991; Rocchi et al., 2003; Salvini et al., 1997). Topographically, the WARS comprises a group of subglacial basins. Among these, the deepest is the Byrd Subglacial Basin (BSB), which contains the lowest point of all continental plates. Another notable region in WANT is the Amundsen Sea Embayment (ASE), the coastal area near the Amundsen Sea. Ice sheet models show that the ASE region holds ~25% of the West Antarctic Ice Sheet (WAIS) within its drainage basins (Larter et al., 2014), and accelerated ice mass loss has been occurring in this region for several decades (Joughin et al., 2014; King et al., 2012). Thus, understanding its mantle seismic structure helps to constrain parameters such as geothermal heat flux and mantle viscosity that are important for cryospheric evolution.

The most notable geographic feature in EANT is the Gamburtsev Subglacial Mountains (GSM). The GSM maintain a high elevation (>2,000 m) in a cratonic geological setting, and their age and origin have been widely debated (e.g., Ferraccioli et al., 2011; Heeszel et al., 2013) although the most recent study summarizes that it is likely has the same age and origin of the East African orogeny (Merdith et al., 2017), but understanding their origin is still fundamentally limited by a complete absence of geological samples. Adjacent to the high GSM, a set of subglacial basins dominates the subice topography (e.g., the Polar Subglacial Basin [PSB], the Wilkes Subglacial Basin [WSB], and Maud Subglacial Basin [MSB]). Their large-scale, internal structure has been constrained by geophysical studies (Ferraccioli et al., 2009; Pyle et al., 2010; Stern & ten Brink, 1989; Studinger et al., 2004; ten Brink et al., 1993), but their origins are not fully understood.

The Transantarctic Mountains (TAMs), one of the major Cenozoic mountain ranges in the world (Robinson & Splettstoesser, 1984), are a 3,500 km-long mountain range with elevations of up to 4,500 m, extending from Northern Victoria Land to the Weddell Sea along the Pensacola Mountains (PMs). The TAM system, together with the Ellsworth and Whitmore Mountains (EM-WM), mark the boundary between the WANT and EANT. The TAM uplift occurs along the flank of the WARS in an extensional environment (ten Brink et al., 1997) and is

Table 1
Seismic Arrays Used in This Study

Seismic arrays/stations	Deployment year	Number of stations used for ANT	Number of stations used for PRF	Additional notes
TAMSEIS	2001–2003	42	33	Across TAM near McMurdo
GAMSEIS/AGAP	2007–2009	28	26	Near the GSM
POLENET/ANET	2008–2015	59	55	Across the west and central Antarctica
RIS/DRIS	2015–2016	34	5	In the RIS, 29 stations atop floating ice shelf
TAMNNET	2012–2015	15	15	In the northern TAM
Other GSN and networks south of S40 latitude	2001–2015	41	10	Other networks include: AI, AU, C, ER, G, GT, MN, PS, YI, YN, AW, and NORSAR. [a]

[a]AI, Argentinean-Italian Network; AU, Australian Network; C, Chilean National Seismic Network; ER, Mt. Erebus Volcano Observatory Network; G, Geoscope Network; GT, Global Telemetered Network; MN, Italian, Terra Nova Bay, TNV; PS, Japanese Pacific21, SYO, Syowa Station; YI, Antarctic Network of Broadband Seismometers; YN, Seismic Experiment in Patagonia and Antarctica; AW, Germany Stations; NORSAR, Norwegian base station Troll.

commonly considered to be a rift-bounding range for the extensional WARS (Behrendt & Cooper, 1991). In addition, associated elastic uplift has been proposed to explain some segments of it (Wannamaker et al., 2017). However, the collapse of a high plateau (Bialas et al., 2007) has also been proposed to explain the topography.

3. Data Analysis

In this section, we describe the data collection and processing procedures used to produce (1) the Rayleigh wave phase and group dispersion maps and their uncertainties and (2) PRFs. Specifically, we demonstrate the high quality of the ANT maps by showing a comparison with maps generated by Heeszel et al. (2016), which were constructed using a completely independent data set determined from teleseismic earthquakes and two-plane wave tomography (2PWT) (Forsyth & Li, 2005; Yang & Forsyth, 2006).

3.1. Seismic Stations in Antarctica

The data used in this study were recorded over the past two decades (Table 1) by a large set of seismic stations throughout continental Antarctica as well as on other land-based stations in the far Southern Hemisphere. These stations include three large temporary arrays that were used by Heeszel et al. (2016): TAMSEIS, AGAP/GAMSEIS, and POLENET/ANET stations deployed before 2013. Additionally, we include 20 new POLENET/ANET stations deployed between 2013 and 2015, which were not incorporated into previous studies. These stations substantially improve coverage in parts of WANT as well as adjacent areas of EANT (Figure 1b). We also use data from 34 stations of RIS/DRIS (Bromirski et al., 2015, 2017; Diez et al., 2016) across the Ross Ice Shelf (RIS) and 15 stations of TAMNNET array (Hansen et al., 2015) in the northern TAMs. All Global Seismographic Network (GSN) stations as well as several from other national networks across the Antarctic continent and south of −40° latitude, are also employed, bringing the total number of stations used in this study to 219 (see Table 1 for details). Station locations on the continent are shown in Figure 1b. It should be noted that for PRF processing, we only use the stations where we have reliable local surface wave dispersion measurements (i.e., the region outlined in Figure 1a by the black dashed line). About 29 stations from the RIS/DRIS array were deployed on the floating RIS where meaningful RFs are not possible, so these stations are not included in the RF processing and subsequent joint inversion, although phase and group velocities from these stations were used in the ANT. In the end, we use RFs from 144 stations.

3.2. ANT and Rayleigh Wave Dispersion Curves

The use of ANT and data from multiple seismic networks to generate high-quality surface wave signals has been shown to be a powerful tool to seismically image other continents (i.e., eastern Asia: Shen et al., 2016). In this study, we follow a similar approach to that study, and therefore, we only provide a summary of the methodology here.

For all 216 seismic stations introduced in section 3.1, we collect the continuous, vertical component seismograms from data recorded between 2000 and 2016. Following Bensen et al. (2007), we cut these seismograms into one-day lengths, deconvolve station responses, decimate to 1 sample per second (sps) if needed, remove earthquake signals between 15- and 50-s period using a moving window technique, and conduct frequency whitening. We compute the daily cross correlations between all possible station pairs. We then stack the cross-correlations and add the positive and negative time components to obtain the symmetric cross-correlation signals. Finally, we perform a frequency-time analysis (Levshin et al., 1972) of the symmetric component of the cross correlation to obtain the phase and group travel times. These phase and group travel times are further selected by two quality control (QC) criteria: they should be made along path lengths greater than three wavelengths, and their signal-to-noise ratio should be >8. The number of good measurements is the largest for periods near 20 s and decreases at both short (<16) and long (>40) periods due to the decrease of signal-to-noise ratio of the Rayleigh waves.

With these QCed surface wave phase and group travel time measurements, we conduct a straight-ray-based tomography (Barmin et al., 2001). The method does not consider the off-great circle path effect and other finite frequency effects, but the bias is small and thus can be neglected in the ambient noise frequency band (Lin & Ritzwoller, 2011; Ritzwoller et al., 2011). It is also likely that some measurements along the structural boundaries are affected by multipath effect. But as many paths perpendicular to these boundaries are also included in the inversion, which are less biased, the overall effect is small. Furthermore, when the resulting phase velocity map is compared with that generated by 2PWT (Heeszel et al., 2016), which does consider multipathing effects and some finite frequency effects, the similarity between the two maps demonstrates that such bias is insignificant at short periods (see the discussion in section 3.3). The straight-ray tomography is performed iteratively, with travel-time measurements discarded during each iteration if their misfit is large (> about 3 standard deviations of the misfit distribution).

Examples of the ANT phase velocity maps are shown in Figure 2. At short periods (12 s), the map is highly heterogeneous, with high velocities beneath parts of the RIS and the ASE. At intermediate periods around 24 s, which are sensitive to mid and lower crustal as well as Moho depths, we observe a strong dichotomy between WANT and EANT, directly reflective of the significant difference in crustal thickness between these two regions. At 36- and 45-s period, which are mostly sensitive to depths of ~ 40–70 km, the dichotomy decays as uppermost mantle Vs variations are revealed in WANT, while crustal thickness variation dominates the phase velocity variations in EANT, especially at 36 s. Figure 2 also presents the contours within which path density is higher than 100 per 40,000 km^2 (dashed line in Figure 2), where the paths are in general dense enough to resolve the regional structures. In this study, we subsequently trim the ANT maps and only retain the measurements that lie within this contour, where horizontal resolution is better than 800 km (more details of the horizontal resolution can be found in the supporting information).

ANT provides two sets of dispersion maps between 8- and 50-s period: phase velocity (example maps shown in Figure 2) and group velocity (shown in the supporting information). In this study, we also incorporate long-period phase velocity dispersion maps obtained by 2PTW from Heeszel et al. (2016), and use all three sets of maps to construct local dispersion curves. As will be discussed in section 3.3 and Figure 3, between 26 and 50 s both ANT and 2PWT provide comparative phase velocity measurements, and we combine them through a linearly varying weighted summation scheme that roughly reflects relative map quality as a function of period:

$$p(T) = \frac{50 - T}{24} \cdot p_{ANT}(T) + \frac{T - 26}{24} \cdot p_{2PWT}(T) \qquad (1)$$

in which p is the phase velocity at period T. At 26 s the ANT data are weighted 1 and 2PWT is weighted 0, and at 50 s ANT data are down weighted to 0 and the weight of 2PWT is weighted 1. The same weighting function is also applied to the uncertainty estimates of the phase velocity. Finally, we thus obtain phase velocity curves between 8 and 143 s. The number of phase velocity measurements varies spatially depending on the quality of the longer and shorter period measurements, so we only retain the dispersion measurements at locations where the number of contributing estimates is greater than 25. The region where the phase velocity curve spans a wide period range (with >25 contributing estimates) is delineated in Figure 1 by the black dashed
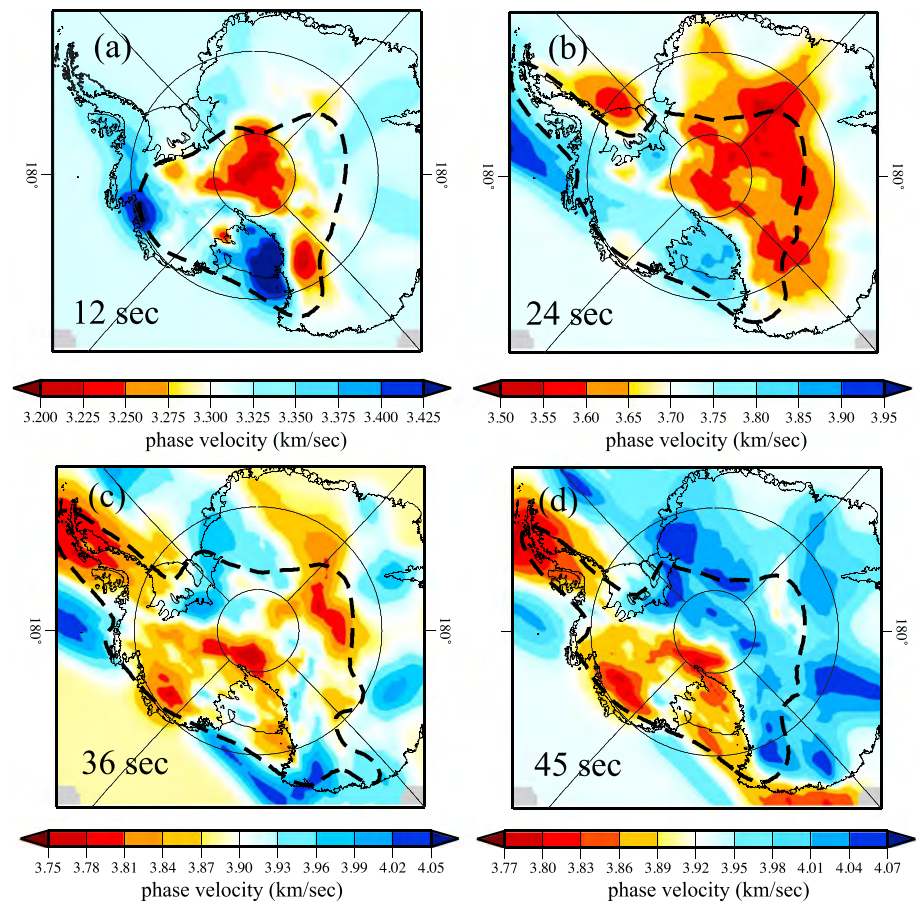
Figure 2. Phase velocity maps determined from ANT. (a) Twelve-second Rayleigh wave phase velocity map across Antarctica. The dashed contour denotes the extension of the region with path density greater than 100 per 40,000 km². This is also largely the region having the best resolution. (b–d) Similar to (a) but for periods of 24, 36, and 45 s, respectively.

line, which defines the area for which we derive the final 3-D shear velocity model. Figure 4a shows an example of phase and group velocity curves for station SWEI.

3.3. Reliability and Uncertainties of the Dispersion Estimates

The consistency of tomography maps can be evaluated by comparing results that are independently constructed using different data and methods. At periods between 26 and 50 s, our Rayleigh wave phase velocity maps generated using ANT can be compared with those previously constructed with data from teleseismic earthquake waveforms using 2PWT (Heeszel et al., 2016). The quantitative differences between these maps at 30-s period are small (Figures 3a and 3b), shown in map view in Figure 3c and as a histogram in Figure 3d. The greatest difference appears near the edge of the maps, and the average difference between the two maps is only 1 m/s (~0.03%), with the standard deviation below 30 m/s (<0.8%). The similarity between the two maps is also observed at other periods. However, below 26 s, the quality of the 2PWT maps is reduced, and at longer periods (~50 s), the ANT maps become less reliable; therefore, in both cases the difference increases. We conclude that the high coherence between the two maps suggests that both sets of maps are reliable and thus can be combined for 3-D shear velocity model construction, with ANT maps used below 26 s and 2PWT maps used at periods longer than 50 s.

We also make a comparative assessment of the uncertainties of the maps. For the ambient noise maps, we estimate the phase velocity uncertainties in two steps: First, we assign the average uncertainties (0.01 m/s) for regions with relatively high path density (greater than 100 paths per 40,000 km²). Second, we scale the uncertainties according to path density for the regions with lower path density with an empirical relationship similar to the approach pursued in earlier surface wave tomography work for eastern Asia, as in Shen et al.,
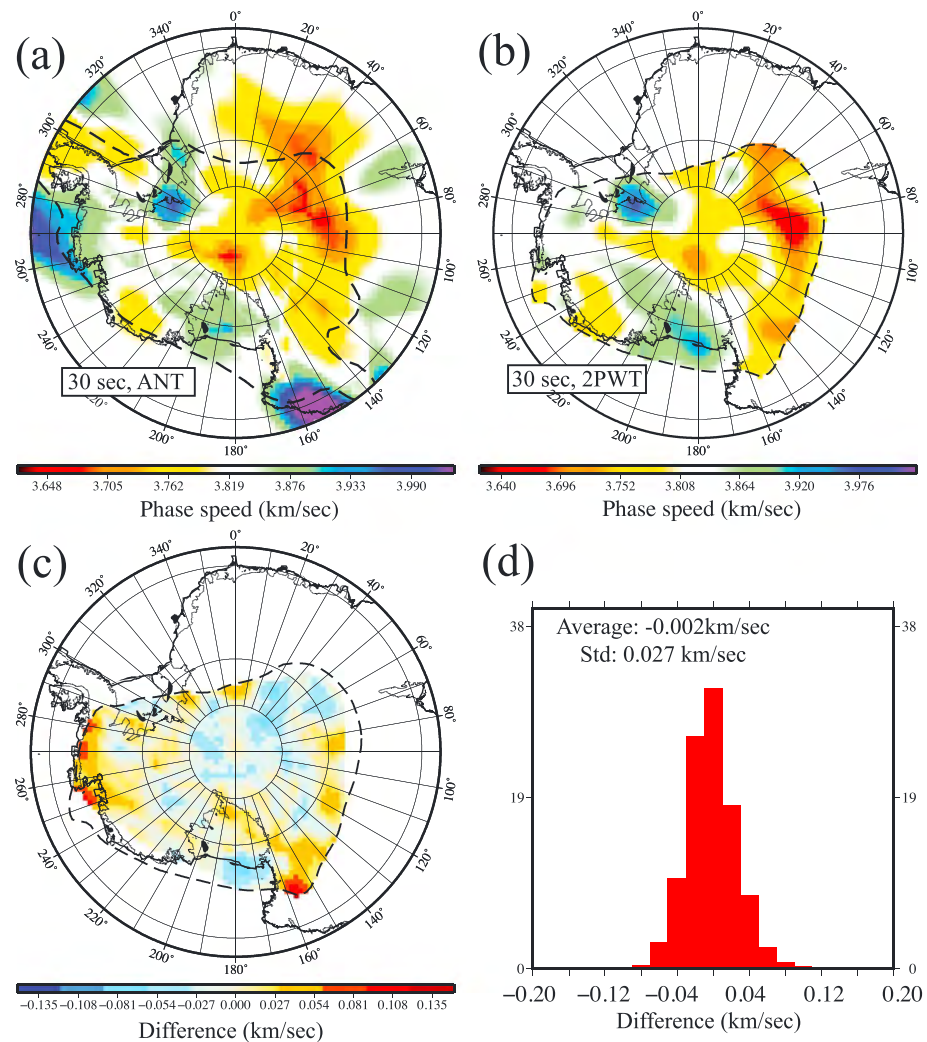
Figure 3. Comparison between ambient noise tomography (ANT) results and two-plane wave tomography (2PWT) results at 30 s. (a and b) Rayleigh wave phase velocity at 30 s from ANT and 2PWT, respectively. (c) Spatial distribution of the difference between maps (a) and (b). Only the regions where ANT result have high path densities (80 per 40,000km^2) and 2PWT has reliable values are shown. The dashed contour outlines the study region, where we have enough surface wave measurements to perform the 3-D model construction. (d) Histogram of the values presented in (c). The average difference is −2 m/s, and the standard deviation is 0.027 km/s.

2016. In that study, the empirical relationship was tested using North America data where uncertainties can be obtained by eikonal tomography, and such relationship should not change from region to region. For long-period phase velocity maps derived from earthquakes, Heeszel et al. (2016) estimated formal uncertainties from the posterior model covariance matrix (Forsyth & Li, 2005). Such calculations underestimate the true uncertainties as they only consider random errors (e.g., they do not reflect systematic biases arising from regularization, which are difficult or impossible to reliably estimate; e.g., Aster et al., 2011), and the Heeszel et al. (2016) uncertainties are much smaller (~0.5 or less) than those determined from ANT. As a rough accommodation for this discrepancy, we adjust the Heeszel et al. (2016) uncertainty estimates upward by a factor of 2. With this approach, the resulting uncertainties of the ANT maps become approximately consistent with the maps derived from teleseismic earthquakes at overlapping periods, and they become consistent with the map differences shown in Figure 3d. By following Moschetti et al. (2010) and Shen and Ritzwoller (2016), group velocity uncertainties are scaled from phase velocity uncertainties by a factor of 2, since the group velocity measurements from ANT are less stable than phase velocity measurements. Here we admit that although we have made rigorous efforts to make measurements of the data uncertainties, they still only represent a quantitative estimate of our confidence in the accuracy of the data.
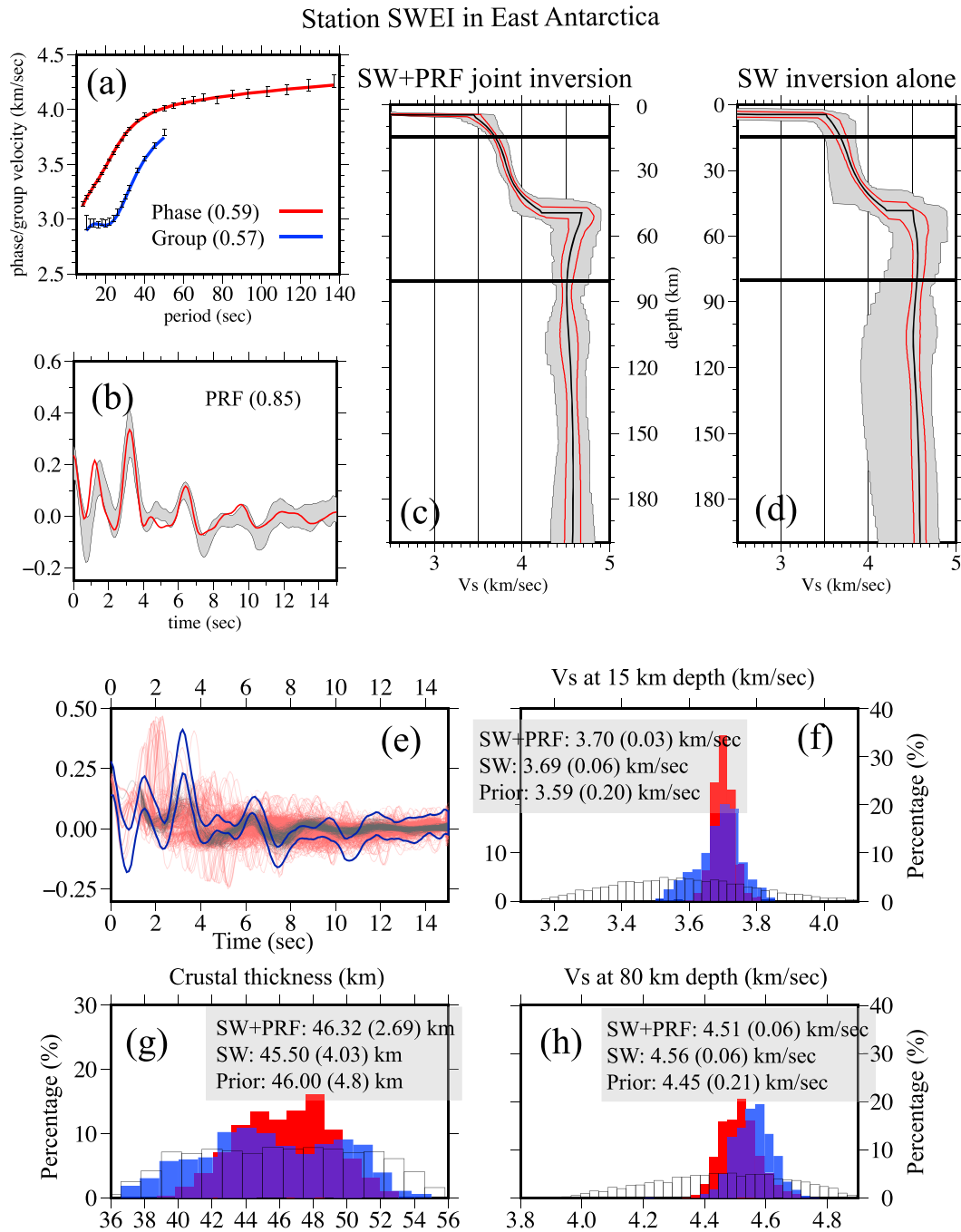
Figure 4. Example of the observed surface wave dispersion and *P* receiver function (PRF) for station SWEI (its location is marked in Figure 1b) in East Antarctica as well as the comparison of the Monte Carlo joint surface wave (SW) and PRF inversion with the SW inversion alone for this station. (a) Observed phase and group velocity dispersion curves for SWEI are shown with 1 standard deviation error bars. The fit from the average model to the observed data is shown as red and blue curves for phase and group velocity curves, respectively, with the square root of the reduced χ^2 misfit values given in parentheses. (b) Observed PRF with uncertainties shown by grey shading. The red curve represents the synthetic PRF from the model shown as the black profile in (c). (c) The resulting 1-D versus ensemble from the joint inversion. The black profile represents the average model, while the two red profiles represent the one standard deviation of the posterior distribution. The full model ensemble fills the grey corridor outlined by black outlines. The fit to data of the average model is presented in (b). (d): Similar to (c) but for the 1-D model ensemble resulting from the SW inversion alone. The red horizontal lines indicate depths for which marginal statistics are displayed in (f) and (h). (e) Receiver functions predicted by the model ensemble shown in (d) are shown as red receiver functions, while those from model ensemble shown in (c) are shown as grey waveforms. The joint inversion of SW and PRF only accepts the models that fit both the observed surface wave dispersion and PRF. Prior and posterior distributions for the Vs at (f) 15 km, (g) crustal thickness, and Vs at (h) 80 km are shown as blank and colored histograms, respectively. Mean and standard deviation for these distributions are presented. Posterior distributions from the joint inversion are shown as red histograms, and those from surface wave inversion are shown in blue.

3.4. PRFs

PRFs are processed following the procedures of Shen, Ritzwoller, Schulte-Pelkum, and Lin (2013) and Shen and Ritzwoller (2016). To process the data, we first collect *P* wave seismic records for earthquakes with Mw >5.5 and distances between 30° and 120°. The seismograms are decimated to 10 sps and are cut with a time window beginning 30 s before and ending 60 s after the *P* arrival. A cosine taper is then applied, and the horizontal components are rotated into radial and transverse directions. The vertical component is then deconvolved from the radial component using a time domain deconvolution algorithm (Ligorría & Ammon, 1999). The deconvolution is performed by an iterative linear-inversion scheme in which 200 iterations are performed and a Gaussian low-pass filter (with Gaussian parameter of 2.5) is used so that the final PRFs have a period of ~1 s. The QC scheme described by Deng et al. (2015) is applied to select out PRFs for back azimuth consistency. In this QC, we remove the PRFs that are not consistent with other PRFs with similar back-azimuths. On average, we retain ~100 PRFs for each station.

Figure 4b shows an example of a stacked PRF waveform with uncertainties defined by its standard deviation of the contributing waveforms. The strongest amplitudes in the 0- to 3-s time window are reverberations generated by the 3-km thick ice layer underlying the station SWEI (e.g., Chaput et al., 2014). These signals have higher amplitude and obscure common Moho-converted phases, such as *P-S* converted phase (*Ps*). The effect of the ice reduces the capability of imaging the deeper seismic discontinuities and thus produces relatively higher uncertainties in Moho depth of the Antarctic 3-D model compared with similar efforts on ice-free continents (e.g., Shen & Ritzwoller, 2016). However, in section 4.2, we demonstrate that the incorporation of PRFs still enables us to provide some constraints on the crustal and Moho structure, compared with surface wave inversion alone.

4. Bayesian Monte Carlo Inversion for a 3-D Model

In this section, we describe the construction of the 3-D Vs model using a Monte Carlo inversion algorithm. A Monte Carlo inversion was first applied to this region with a lower resolution surface wave data sets (Shapiro & Ritzwoller, 2002), but the new model described here incorporates receiver functions and short-period surface wave measurements, which improve the determination of crustal structure. The method used here has been described in detail by Shen, Ritzwoller, Schulte-Pelkum, and Lin (2013) and Shen and Ritzwoller (2016). The fundamental nature of Monte Carlo sampling is that it presents the assumptions, prior constraints, and results as prior and posterior distributions. Here we discuss the Monte Carlo joint inversion using one station (SWEI) as an example, with a focus on improvement over the inversion with surface wave data alone. Additionally, we present the posterior distributions, both for individual stations as well as map views of the distribution means for key model attributes (i.e., crustal thickness and Vs at specific depths). More detailed discussion of the method such as the depth sensitivity of surface wave can be found in the supporting materials.

4.1. Model Space and Monte Carlo Prior Sampling

Monte Carlo sampling is performed in a given model space, dictated by a model parameterization. We here adopt a simple model parameterization following Shen, Ritzwoller, and Schulte-Pelkum (2013). At each location, the 1-D Vs model is parameterized by four layers: an ice layer with ice thickness predetermined from Bedmap2 (Fretwell et al., 2013), a thin sedimentary layer parameterized by a linear Vs gradient, a crystalline crust that is parameterized by four cubic B-splines, and an upper mantle layer that is parameterized by five cubic B-splines to ~300 km. Below 300 km, the model gradually connects to the AK135 Vsv model (Kennett et al., 1995). The peak depth sensitivity of the longest period (143 s) used in this study is between 200- and 300-km depth range, but we also notice that it has sensitivity down to a depth greater than 300 km, and a trade-off between Vs above and below this depth still exists, although neglected in the inversion. In each 1-D model, there are three discontinuities: at the base of ice layer, the base of the sedimentary layer, and the base of the crystalline crust (Moho). Surrounding the continent, the parameterization is modified in two water-covered regions. Beneath ice shelves (e.g., RIS and Ronne Ice Shelf), we insert a subice ocean layer, and in regions of open water, we replace the ice layer by a surface water layer. In both cases, we use the water layer thickness determined by Bedmap2 (Fretwell et al., 2013), zero Vs, *P* wave velocity (Vp) of 1.47 km/s, and density of 1,000 kg/m³. During the inversion we invert for the shear velocity at 1 s using the Qs value from AK135 model for the crust and set Qs to be 150 in the uppermost mantle. Inversions with

different Qs models show that the results are not significantly affected by uncertainties in the Qs model (see the supporting information). In this study, we ignore the radial anisotropy and invert for isotropic Vs structure (Vsv = Vsh = Vs). Because the model velocities are largely constrained by Rayleigh wave dispersion, our final velocity model is overwhelmingly influenced by Vsv.

Based on this parameterization, we define a model space and sample it with a Monte Carlo random walk. The model space is defined by 13 free parameters in total: sedimentary layer top and bottom Vs and its thickness (3), crustal cubic B-spline coefficients and its thickness (5), and mantle cubic B-spline coefficients (5). Such a model space is designed as a perturbation range relative to a predetermined reference model, which is constructed using the local surface wave dispersion inversion. The prior sampling (the Monte Carlo walk without incorporation of any observed data) produces the prior distribution of model ensembles. Example marginal distributions of the prior sampling for model attributes, such as Vs at depths and crustal thickness, are shown in Figures 4f–4h. As we allow a large model space without placing strong prior constraints on the model, the prior distributions are generally broad.

4.2. Constructing the 3-D Model With the Posterior Distributions

At station locations where PRFs were obtained, we perform a joint Monte Carlo inversion of Rayleigh wave dispersion and receiver functions. At each station location, the product of the Monte Carlo inversion is an ensemble of 1-D models resulted from the posterior sampling. The posterior sampling is the Monte Carlo random walk guided by the likelihood functions determined by the misfit to observed data (Bodin et al., 2012; Shen, Ritzwoller, Schulte-Pelkum, & Lin, 2013). If the misfit applies to both the surface wave dispersion and PRF, then the resulting model ensemble is from a joint PRF + SW inversion; if only surface wave dispersion data are used, then we only obtain the SW inversion results.

Figures 4c and 4d present examples of the resulting ensembles of 1-D models for station SWEI that result from the SW inversion alone and from the joint PRF + SW inversion, respectively. With the incorporation of the PRF, the resulting joint model ensemble (Figure 4c) from sampling the posterior distribution is narrower compared with those that result from surface wave inversion alone (Figure 4d), especially for the crust. This is because the joint inversion forces the Monte Carlo model search to reject models that are highly inconsistent with the observed PRF (i.e., many of the red PRF waveforms shown in Figure 4e). The posterior distribution of the crustal thickness (depth to Moho from the bedrock surface), computed from the ensemble of accepted models from the Monte Carlo sampling, narrows noticeably compared to the SW inversion alone. Additionally, the crustal Vs is more precisely constrained: at 15-km depth, the standard deviation of the posterior distribution decreases from 0.06 to 0.03 km/s. For comparison, the posterior distribution of Vs at 80-km depth is largely unchanged (Figure 4h). This improvement depends on the fact that the ice thickness is known, which allows us to impose an accurate prior constraint on this parameter. In total, we obtain 141 stacked receiver functions in our study area (the corresponding stations are shown in Figure 5b).

In the regions where PRFs could not be obtained, either because of the absence of high-quality stations or because stations were on an ice shelf where Moho-converted P-S (Ps) phases are not recorded, we perform Monte Carlo inversion with local dispersion curves. Finally, we construct the 3-D model at a regular (0.5 by 0.5°) grid using a two-step approach: (1) For grid points where a nearby (distance <75-km joint inversion result can be obtained, we use a weighted average scheme to combine the nearest joint inversion result with the surface wave inversion alone result locally. (2) For grid points where there are no seismic stations within the 75-km radius, we retain the 1-D model from surface wave inversion. There are many ways to choose the preferred result from the posterior distributions (e.g., the maximum posterior model and the mean model; Mosegaard & Tarantola, 1995). In this paper, we interpret the mean of the posterior distribution as the best estimate of the Vs structure and Moho, given that the distributions of Vs at each depth are mainly Gaussian (Figures 4f–4h), and the corresponding covariance is used to estimate the uncertainty.

5. Results

In this section we present the map views of some key attributes of the 3-D model. Maps of crustal thickness and its uncertainties are presented in section 5.1. In section 5.2, we present some horizontal sections of the 3-D model, extending from depths in the shallow crust to those in the uppermost mantle.
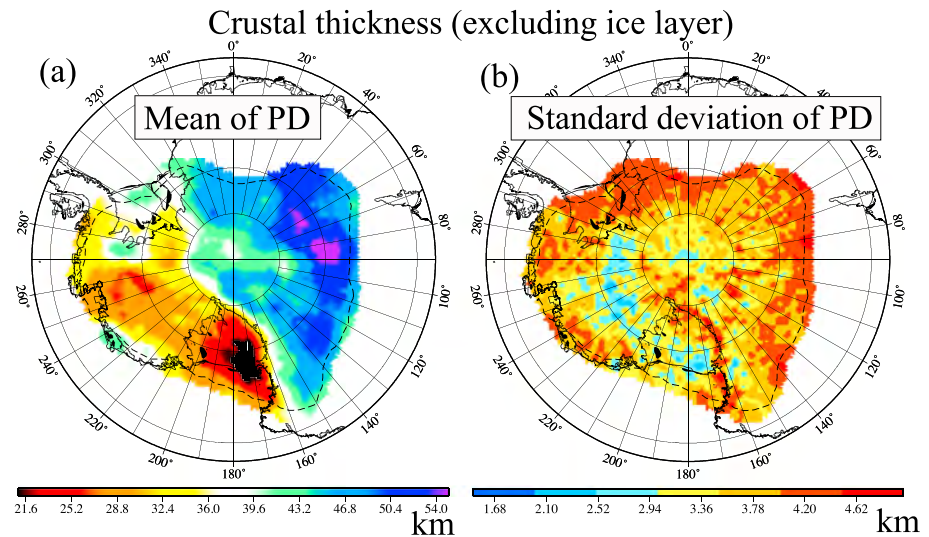
Figure 5. Map views of the posterior distribution (PD) for crustal thickness. (a) Map view of the mean of the PD. (b) Map view of the standard deviation of PD.

5.1. Crustal Thickness

A map of the mean of the posterior distribution for the crustal thickness is shown in Figure 5a. The thickest crust ($>$55 km) is observed beneath the GSM, which is consistent with earlier seismic studies based on S wave receiver functions (Hansen et al., 2010) and surface wave dispersion (An et al., 2015; Heeszel et al., 2013). Generally, the spatial variations of crustal thickness are also similar to those estimated by gravity studies (e.g., Block et al., 2009), but the absolute crustal thickness of the seismic estimates in EANT are up to 10 km thicker. The TAMs are broadly characterized by an extremely large horizontal crustal thickness gradient: changing from thicknesses of 45–48 km on the EANT side of the range to 20–30 km beneath WANT, consistent with previous more localized studies in the Ross Sea area and the northern TAMs (Finotello et al., 2011; Hansen et al., 2009, 2016; Lawrence et al., 2006c; Stern & ten Brink, 1989). The thinnest crustal thickness is found beneath the TAMs side of the RIS ($<$20 km), while the Siple Coast side of the ice shelf is relatively thicker (~25–30 km).

The standard deviation of the posterior distribution for crustal thickness (Figure 5b) provides an estimate of the model uncertainty. On average, regions with thin crust show smaller standard deviation in crustal thickness as well. The incorporation of receiver functions yields lower standard deviation (~3 km) in crustal thickness near station locations. For comparison, joint inversion-derived uncertainties of crustal thickness for the United States are ~1–2 km for regions with clear receiver functions (Shen, Ritzwoller, & Schulte-Pelkum, 2013, Shen & Ritzwoller, 2016). The lower crustal thickness resolution obtained in Antarctica is likely due to the reverberations from the ice layer in the Antarctic PRFs. One notable feature of the map is the relatively high standard deviation along the TAM front. This reflects complex lateral Moho and/or crustal structure, as is indicated by individual PRF analysis (Ramirez et al., 2017).

5.2. Horizontal Slices of the 3-D Model

The Vs model exhibits a number of major structural features, revealed in the horizontal slices at various depths (Figures 6 and 7). At shallow depths (Figure 6), shear velocity variations mostly reflect the thick sedimentary basins and variations in crustal thickness. At ~8-km depth below the top of ice (which is ~5–6 km below the surface of the bedrock), Vs displays a distinguishable difference between EANT, EM-WM-TAMs, and WANT. In general, shallow Vs is slower west of the high TAMs, whereas Vs is higher to the east, with the fastest region in EANT concentrated near the GSM. One can speculatively associate the high velocities in the GSM with the shallow exposure of metamorphic rocks by mountain uplift and erosion, as is observed for the shallow Vs structure beneath the Sierra Nevada and Front Range Rocky Mountains in North America (Shen, Ritzwoller, & Schulte-Pelkum, 2013). The slowest Vs is found beneath the Ross Embayment, in accord with previous seismic studies, in which 2- to 8-km thick sediments in this region are reported (Lindeque et al.,
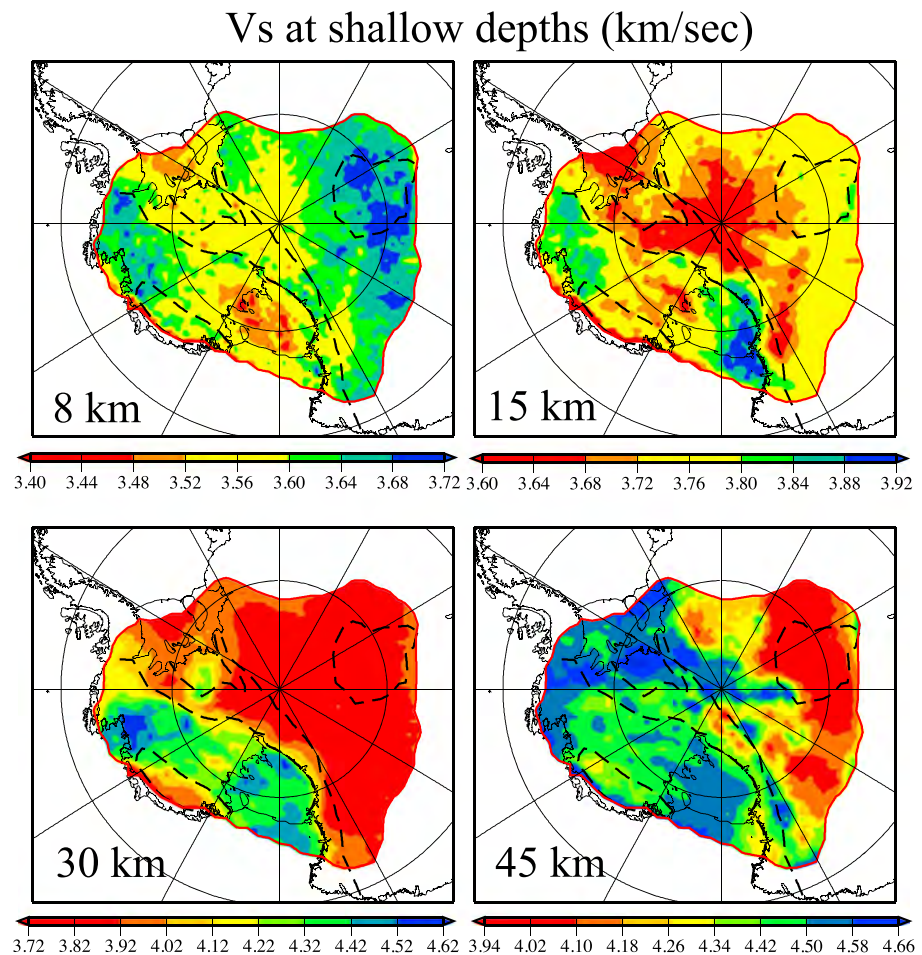
Figure 6. Horizontal slices through the 3-D Vs model. (a) Average Vs at 8-km depth, computed by averaging Vs between 5- and 11-km depth, representing the Vs in the upper crust. (b) Vs at 15-km depth, computed by averaging Vs between 12- and 18-km depths. (c and d) Same as (b) but for Vs at 30- and 45-km depths, respectively.

2016). At ~15-km depth, slow Vs is generally found beneath the Whitmore-Ellsworth Mountain (WM-EM) ranges and near the South Pole. Another notable region with slow midcrust Vs is to the east of the TAMs near Ross Island.

At 30- and 45-km depth (Figures 6c and 6d), Vs largely reflects the variations in Moho topography. At 30-km depth, the fast (uppermost mantle) Vs is seen beneath the WARS and the lowland areas between the WM-EM ranges and the PMs consistent with thinner crust. In contrast, crustal Vs values (~3.7–4 km/s) are found beneath EANT. At 45 km, the fast velocity beneath most of WANT indicates a lithospheric mantle lid (Vs ~ 4.3–4.4 km/s) near this depth, especially around the Ross Embayment (Heeszel et al., 2016; O'Donnell et al., 2017). Conversely, velocities of less than 4 km/s observed beneath the GSM at 45-km depth are consistent with the Moho being considerably deeper in this region.

In the uppermost mantle, the dichotomy between EANT and WANT dominates the variations in Vs (Figure 7), which again reflects the seismic signature of the cratonic nature of EANT versus the Mesozoic/Cenozoic extensional WARS. At 60-km depth (Figure 7a), the slowest Vs is found beneath the TAMs and MBL. Vs beneath the TAMs and MBL is further reduced to sublid velocities below 4.2 km/s at 80 km, and these features are revealed to be connected across the WARS at 120 km, forming a ring-shaped anomaly in the uppermost mantle that encircles a faster region beneath the eastern Ross Sea coast. A slow anomaly beneath the GSM is also seen at 80 km (Figure 7b), which will be discussed in section 6.4. At 160-km depth, the EANT-WANT dichotomy is observed with a horizontal Vs discontinuity along the TAMs-WARS boundary, and the Vs beneath the high TAMs is more consistent with the EANT Vs.
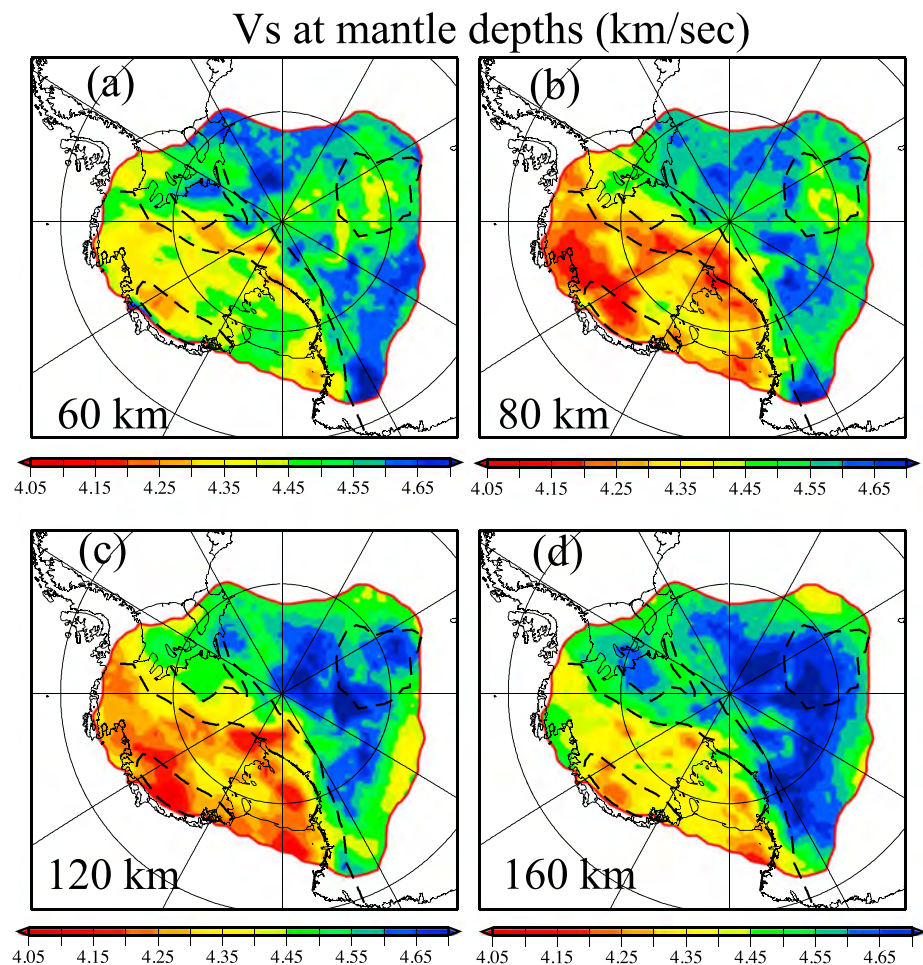
Figure 7. Map views of the 3-D model at uppermost mantle depths.

Notably, as the Bayesian Monte Carlo method is used to produce the 3-D model, standard deviations of the posterior distribution for any attribute (e.g., crustal thickness, Vs at depths) provide assessment to the its uncertainty level. On average, the one standard deviations of crustal and mantle Vs are ~0.03–0.05 km/s (~1%) and ~0.05–0.065 km/s (~1–1.3%) respectively, which are much smaller than the variations displayed in the maps (±5%; Figures 6 and 7). These uncertainties consider both the uncertainties in data as well as the depth trade-off in surface wave inversion but do not include systematic errors due to assumptions in the Q model and Vp/Vs ratio.

6. Discussion

In this section, we discuss the notable features observed in the 3-D model. These include the seismic structures (1) along the WARS-TAMs region, (2) beneath MBL and the ASE, (3) beneath the WM-EM system, and (4) beneath the GSM. These anomalies are mainly in the upper mantle. As discussed in section 5.2 and in the supporting material, if the variations are stronger than 2%, they cannot be caused by bias due to the uncertainties in Moho depth and ad hoc prior assumptions on crustal Vp/Vs, density, or Q structure (Dalton et al., 2008, Lawrence et al., 2006b). Some of the features discussed here are imaged for the first time (i.e., the low-velocity upper mantle beneath the GSM and velocity variations along the TAM and EM-WM). In addition, although aspects of some features discussed in this manuscript have been shown in parts of Heeszel et al. (2016) and An et al. (2015; i.e., the slow anomalies in the upper mantle along the TAM front and near the MBL), they are more clearly imaged and thus can be more completely interpreted in this paper. The discussion is accompanied by the presentations of the average uppermost mantle Vs (Figure 8) and vertical transects across the study region (Figures 9 and 10).
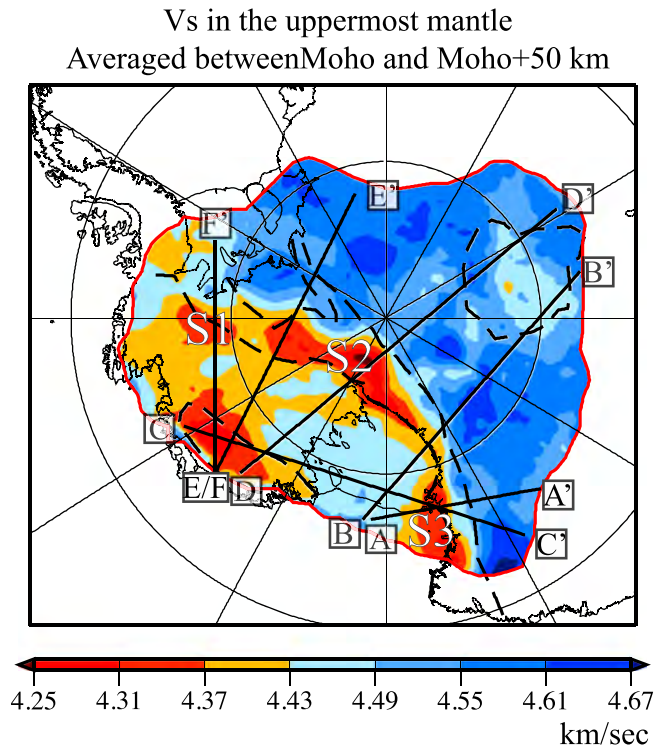
Vs in the uppermost mantle
Averaged betweenMoho and Moho+50 km

Figure 8. Uppermost mantle Vs beneath central and West Antarctica. The map shows the mean of the marginal posterior distribution for Vs between the Moho and 50 km below the Moho. The locations of transects A-A′ to F-F′ (shown in Figures 9, 10) are marked by solid black lines. Slow anomalies S1–S3 are discussed in section 6.1.

6.1. Upper Mantle Structure of the WARS and TAMs

Figure 8 presents the Vs in the uppermost mantle, defined as the average Vs between the Moho and 50 km below the Moho (Moho + 50 km). The most prominent feature is a low-velocity belt along the WARS-TAMs boundary, extending from the Ross Embayment to the EMs. The width of the belt varies from <50 km (near the eastern RIS coast) to greater than ~ 250 km (along the southern TAMs), with an average width of ~100 km. Along the low-velocity belt, the uppermost mantle velocity is generally slower at three regions: the northern TAMs, southern TAMs, and EM. In Figure 8, these anomalies are marked as S1, S2, and S3, respectively. The upper mantle Vs reduces to a minimum of <4.25 km/s near the southern TAMs (S2). In addition, relatively fast Vs is found beneath the WARS near the Siple Coast and Ross Embayment. In this section, we discuss the geographic distribution and tectonic implications of these features in detail.

The slow uppermost mantle anomaly (anomaly S2) is particularly broad beneath the Southern TAMs. This feature has been observed in lower resolution by Heeszel et al. (2016), who noted that the lithosphere is missing in this region, perhaps due to either rifting or delamination. As seen most clearly in transect D-D′ in Figure 10, a wedge-shaped uppermost mantle anomaly beneath the WARS and TAM front extends ~300 km into EANT, coherent with the high plateau east of the TAMs crest. This wedge-shaped anomaly is accompanied by an inclined fast anomaly, which directly connects to the high Vs lithosphere beneath EANT. Beneath the wedge-shaped slow anomaly, the top of the fast upper mantle is located ~160 km beneath the surface and ~110 km beneath the Moho, remarkably deeper than the high-velocity lid (HVL) beneath EANT. Additionally, the slowest velocities of the uppermost mantle are beneath the only area with Cenozoic volcanism located on the EANT side of the TAM front, at Mount Early and Sheridan Bluff (LeMasurier, 1990; Stump et al., 1980), and extending farther into EANT (Licht et al., 2018). By synthesizing these seismic
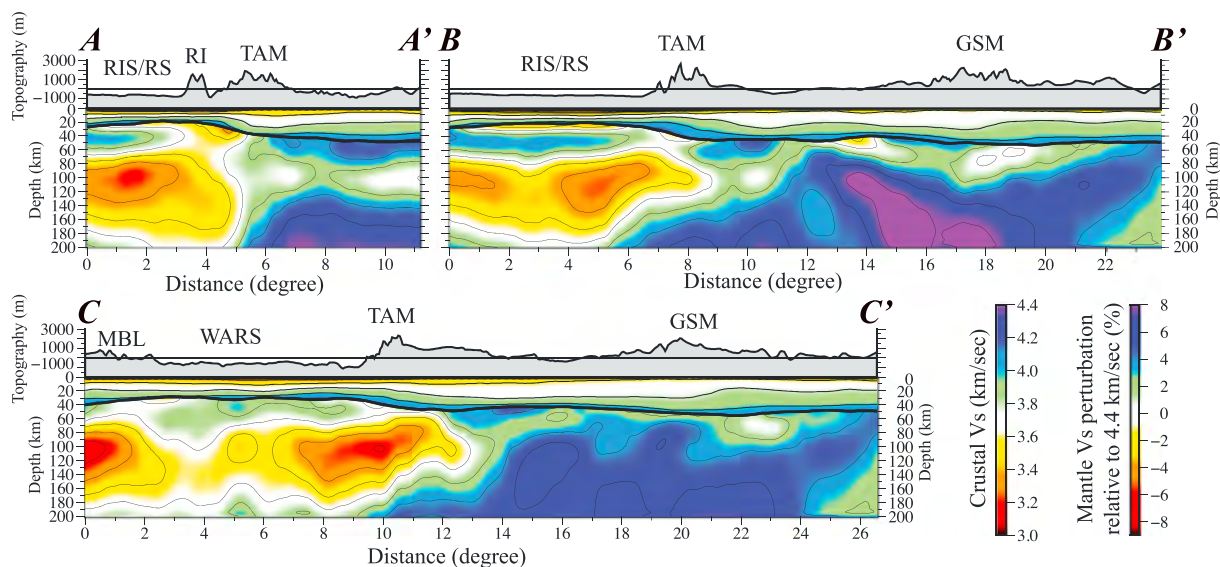

Figure 9. Vertical slices of the 3-D model. Vs structure along transects A-A′ (a), B-B′ (b), and C-C′ (c) for which the locations are marked on Figure 8. The crustal Vs is plotted with absolute values and the mantle is shown as percentage perturbation relative to 4.4 km/s. RE, Ross Embayment; RI, Ross Island; TAMs, Transantarctic Mountains; GSM, Gamburtsev Subglacier Mountains; MBL, Marie Byrd Land; WARS, West Antarctic Rift System.
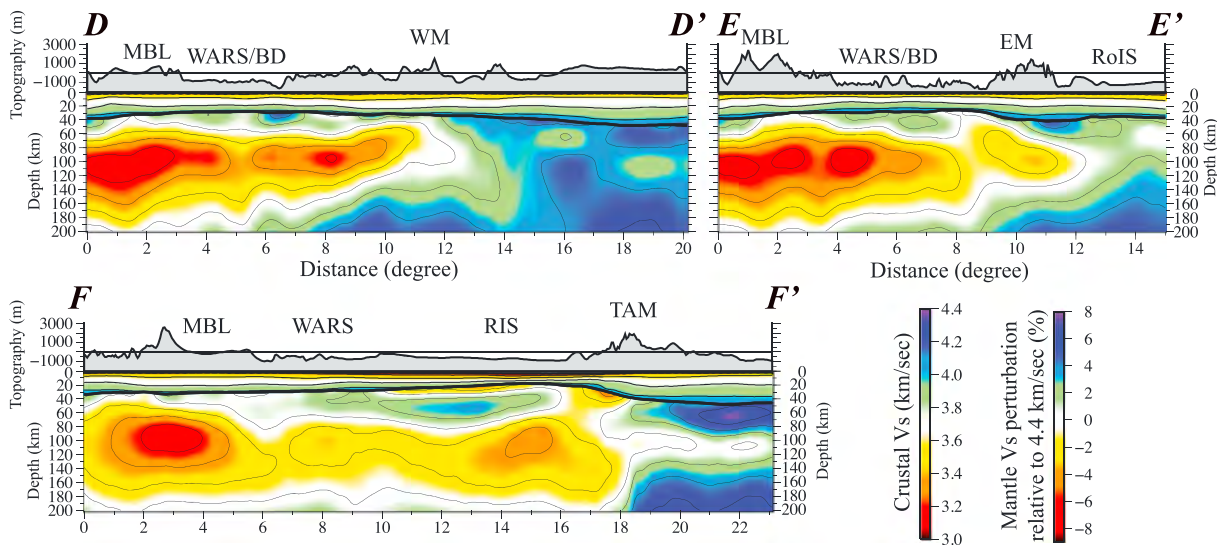
Figure 10. Vertical slices (cont.). Similar to Figure 9, Vs structure along transects (a) D-D′, (b) E-E′, and (c) F-F′ for which the locations are marked on Figure 8. Two vertical lines in EE′ indicates the boundary of a broad region of WM-TM-PM systems that is discussed in section 6.3. BSB, Byrd Subglacier Basins; WM, Whitmore Mountains; TM, Thiel Mountains; PM, Pensacola Mountains; EM, Ellsworth Mountains; RoIS, Ronnie Ice Shelf.

images and geological evidence, we interpret this feature as evidence of active lithospheric foundering, and its possible timing and initiation mechanism have been discussed in a separate paper (Shen et al., 2018).

One question is whether the lithospheric foundering model discussed in detail by Shen et al., 2018 can be applied to other sections of the TAMs (e.g., the central and northern TAMs) and WM-EM ranges. Similar wedge-shaped slow anomalies are also observed in transect B-B′ (Figure 9) near the central TAMs and E-E′ crossing WM and Thiel Mountains, indicating possible lithospheric foundering beneath these regions. To further illustrate the spatial distribution of the lithospheric foundering, the Vs difference between the uppermost mantle and at greater depths (i.e., at 200 km) is presented in Figure 11. Ongoing lithospheric foundering (i.e., the relatively cold, foundering lithosphere beneath the upwelling relatively warm, thus seismically slow, asthenosphere) implies that the uppermost mantle Vs is substantially slow (i.e., <4.4 km/s), and Vs at greater depths (e.g., at 200 km) is much higher. Therefore, the area with positive velocity difference (>0.2 km/s) in Figure 11, which extends along the TAMs front from the northern RIS at ~80°S to the WM, together with the slow uppermost mantle Vs in Figure 8, highlights the possible spatial distribution of lithospheric foundering.

A recent magnetotelluric geophysical sounding investigation (Wannamaker et al., 2017) reveals a thick layer (~200 km) of high electric resistivity beneath the central TAMs near 84°S, which is at the northern end of the slow uppermost Vs (anomaly S2 in Figure 8). Such a high resistivity feature is interpreted as a thick, cold, undisturbed lithosphere (Wannamaker et al., 2017), which suggests a possible sharp boundary between the lithospheric foundering beneath the southern TAMs and a cold, stable lithosphere beneath the central TAMs. Wannamaker et al. (2017) further suggest that a cantilevered flexure mechanism, without strong thermal components, may play a significant role in the uplift history of this region of the TAMs, although broader 3-D seismic structure indicates that such a mechanism would be geographically limited. For example, transect B-B′ shown in Figure 9 exhibits a similar wedge-shaped uppermost mantle slow anomaly near the 82° south section of the
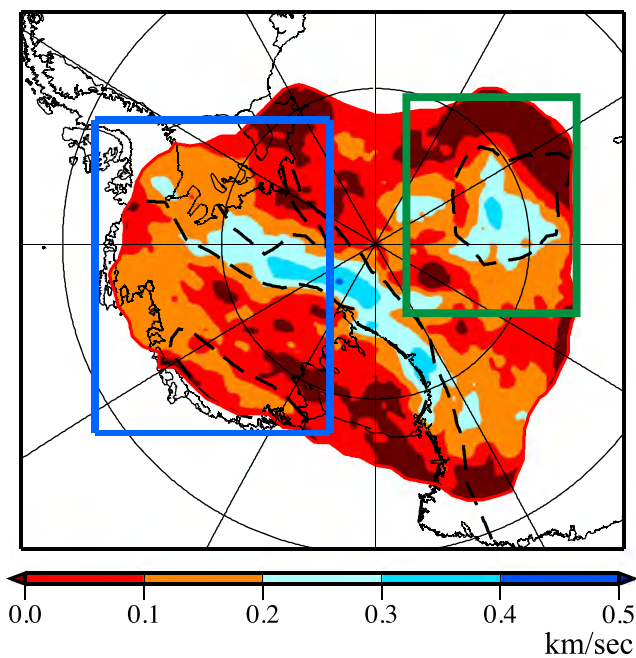

Vs (200km) - Vs (uppermost 50 km of mantle)

Figure 11. Difference between Vs at 200-km depth (calculated by averaging Vs between depths of 180 and 220 km) and in the uppermost 50 km of the mantle (Figure 8). The blue and green boxes highlight the focus regions discussed in sections 6.1–6.3 and 6.4, respectively.

central TAMs. Although this anomaly does not extend into the EANT as far as 400 km like the southern TAMs, it still lies beneath the highest elevation along this transect, suggesting an elevated uppermost mantle temperature which naturally uplifts the TAMs.

In addition to S2, slow anomalies S1 and S3 in WANT near the EMs and northern TAMs (along the Ross Embayment), respectively, are also slower than 4.37 km/s. Horizontally, unlike S2, these anomalies mainly locate within the WARS, extending within 100 km of the high elevation of EM and TAMs fronts. Near anomaly S1, a recent surface wave investigation (Graw et al., 2016) of the uppermost mantle structure also observes anomalously slow uppermost mantle beneath this region, extending ~100–200 km inland from the TAMs front. That study suggests that the low Vs reflects elevated rifting-related temperature and decompression melting. Our results, shown in transects A-A′ and C-C′ in Figure 9, are in general consistent with Graw et al., 2016. Along transect F-F′, crossing the anomaly S3 near the EM, the slowest anomaly near the Moho corresponds to the lowest topography of the BSBs (i.e., near the Bentley Subglacial Trench). It connects with slow Vs observed at the 60- to 120-km depth range beneath the EM, but with a weaker amplitude (only ~ −2 to −4% relative to the average Vs across the study area) compared with the slow anomaly beneath southern TAMs (~6–10%). Below this slow anomaly, a relatively fast anomaly is seen at depths >120 km. Given the weak amplitude of the slow Vs anomaly, it is difficult to distinguish whether it may be caused by horizontal heat conduction or a lithospheric foundering, but the relatively high velocity at greater depths suggests that perhaps the later is more plausible. In summary, the upmost mantle slow anomaly belt (S1 through S3) along the WARS-TAMs, southern TAMs, and WARS-EM/WM front exhibits the lithospheric modification associated with either the rifting of WARS or the rifting-related lithospheric delamination processes. The seismic images of this WARS-front belt indicate an absence of thick lithosphere and subsequently suggest possible high surface heat flow near these regions.

Another notable feature beneath the WARS region is the existence of a variable-thickness high velocity mantle lid across much of the region. Shown in Figure 8, a relatively HVL with Vsv ~4.45 km/s in the uppermost mantle is found encompassing the eastern Ross Embayment and Siple coast region, extending into the lowland basins (e.g., the BSBs) of the WARS. Outside of these areas, Vs is low beneath both the TAMs-EM-WM belt and MBL (<4.35 km/s) region. This HVL is observed in all six cross sections (A-A′ through F-F′; Figures 9 and 10). In transects A-A′, B-B′, and C-C′ crossing the lid beneath the Ross Embayment, this HVL develops eastward of the northern TAMs, with peak Vs greater than ~4.52 km/s at ~50-km depth beneath the central RIS/RS. Along transects D-D′ and E-E′, the lid separates the uppermost mantle anomaly beneath MBL from the rifting shoulder of WM and EM at depths between the Moho and 60 km. This extensively distributed HVL may represent lithosphere that has cooled since the major WARS rifting episodes of the late Mesozoic (Siddoway, 2008). Additionally, this cooling lithosphere layer, although thin, provides an upper bound of surface heat flow of the WARS, especially in the eastern Ross Embayment and Siple coast area. It is notable that the HVL is slower (~4.4 km/s) in the vicinity of MBL than beneath the Ross Embayment, which perhaps is due to the conductive heating by higher temperature mantle near MBL. Origins and implications of the features discussed here call for further data collection and analysis. For the feature beneath the TAM, further geodynamic modeling is needed to evaluate its impact to the uplift history and heat flow. A similar approach could be applied to the cooling plate observed beneath the WARS in the uppermost mantle, which will clarify the extension history of the rift.

6.2. Seismic Structure Beneath the MBL and ASE

Seismic structure beneath MBL is distinct from other regions of the WANT. At 30-km depth (Figure 6c), MBL is seen as a slow anomaly compared to the WARS, as the crust beneath MBL is 5–10 km thicker than the WARS (Figure 5a), in agreement with earlier PRF studies (Chaput et al., 2014; Ramirez et al., 2017). The thickest crust beneath MBL exceeds 36 km, but with a large thickness uncertainty estimate (>5 km) as it is located at the periphery of our study region. In the upper mantle, MBL consistently shows a slow anomaly throughout all depths. In the shallowest mantle (~60-km depth; Figure 7a), Vs is 4.25–4.35 km/s, with the very modest anomaly consistent with a thin lithospheric lid in this region. At 80- to 120-km depth the anomaly is much more pronounced and is centered beneath the highest elevation of the MBL dome. This small-scale variation within MBL continues throughout all depths (Figures 7b–7d) and can be clearly identified beneath the transect C-C′ (Figure 9c). Below 150 km, the anomaly persists, with an amplitude of ~2% slower than WARS and 4–8% slower than the EANT mantle, consistent with body wave tomography studies of the region (e.g., Lloyd
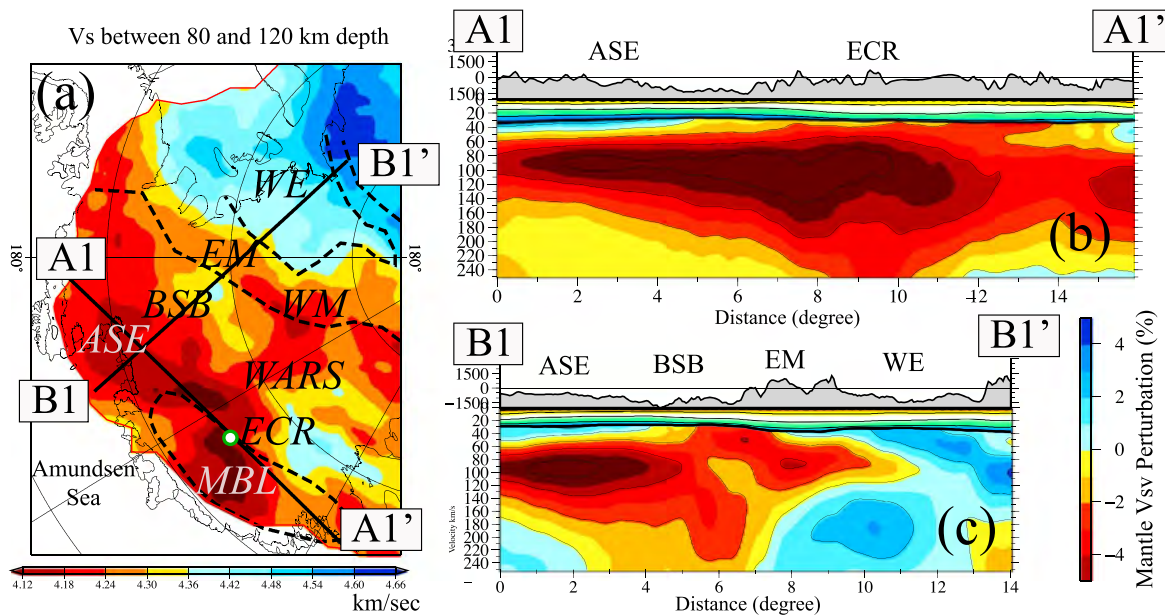
Figure 12. Upper mantle structure near the Marie Byrd Land (MBL) and Amundsen Sea Embayment (ASE). (a) Map view of the average Vs between 80- and 120-km depths. Location of the two transects A1-A1′ and B1-B1′ are marked by two solid lines. The green circle denotes the location of the subglacial volcano found at the Executive Committee Range (ECR). (b) Transects along A1-A1′ whose location is shown in (a). Mantle Vs is shown as percentage perturbation relative to the average 1-D mantle Vs profile of the whole study region. (c) Similar to (b), but for transect A2-A2′. ASE, Amundsen Sea Embayment; BSB, Byrd Subglacial Basins; EM, Ellsworth Mountains; WM, Whitmore Mountains; WARS, West Antarctic Rift system; MBL, Marie Byrd Land.

et al., 2015). The slow anomaly is confined within MBL at ~160–200 km (Figure 7d). Below 200 km where the sensitivity of surface wave degrades, it is unclear whether this anomaly continues deeper into the uppermost mantle. Its detailed linkage to midmantle low velocity anomaly, as noted by Phillips et al. (2018), is not constrained by this study.

Figure 12 presents a set of expanded images of the MBL for the upper mantle. At ~100 km depth, the LVZ reaches its lowest Vs value (4.1–4.15 km/s) near the Executive Committee Range, where an active subglacial midcrustal magmatism has been identified from seismicity (Lough et al., 2013). Maximum velocity anomalies of 4–5% with respect to the surrounding WARS are similar to that estimated using *S* body wave tomography by Lloyd et al. (2015), but the surface waves give an improved estimate of anomaly depth. This indicates high MBL uppermost mantle temperatures that are consistent with a 200–300 °C temperature difference with respect to the surrounding WARS (e.g., Faul & Jackson, 2015). Small amounts of partial melt, associated with the MBL volcanic systems, may also contribute to the seismic anomaly. The seismic signature is consistent with other studies suggesting a weak mantle plume, causing the MBL thermal anomalies and volcanism (e.g., Accardo et al., 2014; Seroussi et al., 2017), in that the velocity anomalies near the center of the dome are stronger and extend deeper than surrounding areas. At greater depth (>200 km), body wave tomography (i.e., Emry et al., 2015; Hansen et al., 2014) provides better images of this region, which suggests the presence of a possibly secondary plume structure.

This study also resolves major low-velocity anomalies near the ASE. This region, along with the BSB, shows thinner crust than most of WANT (Figure 6a), suggesting that the geological history involves major tectonic extensional events. As noted in Figure 12, the upper mantle from the ASE to near MBL also exhibits slow Vs. Along the transect A1-A1′ (Figure 12b), the low velocity beneath the ASE is seen to be connected with the slow Vs anomaly beneath the MBL, which roots to depth near 200 km. Moreover, the slowest Vs in the upper mantle beneath the ASE is confined between ~70 and 130 km depth in the mantle, with the slowest value ~4.15 km/s (~6–7% below the average Vs across the region). Beneath the BSB (B1-B1′, Figure 12c), the slow anomaly extends deeper and its amplitude is reduced to ~ −2-3%. Similar to MBL, we attribute these anomalously low shear velocities to a higher mantle temperature, indicating the presence of a shallow asthenosphere and thin lithosphere. A recent larger-scale seismic study (Lloyd et al., 2017) shows that these anomalies extend along the coastline toward the Antarctic Peninsula and also offshore beneath the

adjacent ocean basins. Considering that this area holds ~25% of the WAIS within its drainage basins (Larter et al., 2014), the slow Vs, together with the thin crust and lithosphere, have a particular importance for the possible linkage between future Antarctic ice sheet collapse rate and mantle viscosity-mediated GIA (Gomez et al., 2015). Recent observations of extremely rapid uplift caused by GIA can only be modeled with very thin lithosphere and low-viscosity upper mantle (Barletta et al., 2017), consistent with the findings presented here.

6.3. Seismic Structure Near the WM-EM and PM Systems

Near the Thiel Mountains, the high elevations of the TAMs bifurcate into two mountain systems (Figure 1a). One branch extends along the Whitmore Mountains to the Ellsworth Mountains (WM-EM system), and another extends to the PMs (PM system), with the two ranges separated by the drainage basins flowing into the Ronne Ice Shelf. The WM-EM region represents a Precambrian terrain originally located between the EANT and African cratons that rotated into place during the breakup of Gondwana (Dalziel, 2007).

At shallow depths, several distinct seismic features are observed in this region. The crust between the two mountain ranges is much thinner than adjacent crust in the Ellsworth Mountains and EANT (Figure 5), and the thin crust likely extends farther north beneath the Ronne Ice Shelf (RoIS) given the low topography there. This feature can be observed directly in the 20- to 36-s surface wave velocity maps (Figures 2 and 3). Crustal thinning in this region is also compatible with gravity results indicating thinner crust and likely results from extension accompanying the opening of the Weddell Sea during the Jurassic (Jordan et al., 2013). The crustal thickness of approximately 40 km beneath the EM is considerably thicker than beneath the WM (~30–33 km), perhaps due to a combination of (1) the fact that the EM are in the core of the Gondwanide orogeny and may have had a deeper crustal root and (2) a disruption of the WM by the thinning process. The middle crust beneath the WM-EM is also slower than in adjacent regions, possibly indicating a more felsic composition, as suggested from body wave tomography by Lloyd et al. (2015). We note that the northern areas of this region are near the edge of our study area due to a scarcity of regional seismic stations, so the uncertainties of the model are higher (e.g., Figure 5b).

In the shallow mantle, to ~120-km depth, the WM-EM system shows a much different structure from the PM branch of TAMs. In general, the WM-EM terrain is prominently slower than the PM and the lowland between the two ranges (Figures 7a–7c). The slower velocity indicates a warmer uppermost mantle, consistent with evidence of younger volcanism in the vicinity of WM-EM (Behrendt & Cooper, 1991). The slowest region, at 80-km depth (Figure 7b), is continuous with slow regions along the TAMs front and beneath the Southern TAMs, suggesting a link between TAMs and WM-EM uplift. Additionally, the slowest anomaly in the uppermost mantle is located beneath the Bentley Subglacial Trench adjacent to the WM-EM, which may be the location of a late Cenozoic rift (Lloyd et al., 2015). At depths >160 km, the region between the PM and WM-EM is considerably faster than the WARS, suggesting that this area is distinctly different in structure and geological history from the WARS. The faster mantle velocities are consistent with a greater age of last tectonic activity for this region relative to the WARS. Specifically, the area between the PM and WM-EM underwent extension during the Gondwana breakup during the early Cretaceous (Grunow et al., 1991), whereas the WARS has been tectonically active during the Cenozoic (Cande et al., 2000; Granot et al., 2010). Also notably beneath the WM, a slow uppermost mantle anomaly is found between 60- and 120-km depths (Figure 10 transect EE′), indicative of a possible mantle foundering beneath this region as well.

6.4. Seismic Evidence of Compositional Variation in the Upper Lithosphere Beneath GSM

The GSM is a broad region (>160,000 km^2) of high topography (greater than 2,000 m) in EANT (Figure 1a). Imaged by S wave receiver functions and by surface waves (Hansen et al., 2010; Heeszel et al., 2013, and this study), the GSM shows the thickest crust beneath Antarctica (~55 km). The implication from seismic studies is that the elevated topography is isostatically supported by thick crust. In contrast, gravity-derived Moho depth beneath the GSM is thinner (Block et al., 2009), but if a different crustal-mantle density contrast is assumed, it is consistent with the seismically derived Moho (O'Donnell & Nyblade, 2014). The difference between these results may come from the different definitions of Moho (i.e., the seismic Moho versus the petrologic Moho). Alternatively, it may be due to an unusually dense deeper crustal root (Ferraccioli et al., 2011) or an anomalous density excess in the uppermost mantle. As seen in Figure 8, a relatively low velocity in the uppermost mantle is observed in EANT. Figure 13 presents an enlarged view to this feature. Beneath the GSM, the

slowest velocity in the uppermost 50 km of the mantle is ~4.45 km/s, which is more than 2% slower than surrounding regions of EANT (~4.55–4.6 km/s), and about 3% slower than the velocity beneath the GSM at greater depths (i.e., ~4.65 km/s at depths >110 km). This feature is also seen in vertical transects crossing the GSM region (transects BB′ and D-D′ shown Figure 9, but more clearly in transects 1-1′, 2-2′, and 3-3′ in Figure 13). The east side of the anomaly is close to the boundary of our study region, so whether it extends out of the study region is unknown. Notably from vertical transect 1-1′ (Figure 13b), this anomaly is approximately centrally positioned near the highest elevations of the GSM; thus, we refer to it as the GSM anomaly hereafter. Below, we argue that the GSM anomaly bears a compositional origin and perhaps a high-density zone between the Moho and ~110-km depth that can perhaps reconcile gravity and seismic observations.

Shear velocity in the uppermost mantle has a high trade-off with estimates of Moho depth (Shen, Ritzwoller, & Schulte-Pelkum, 2013), and the GSM anomaly is observed right beneath the Moho, so its reliability needs to be tested. We thus perform two additional Monte Carlo inversions for a point located within the slow anomaly, but with different prior constraints in Moho depth. Particularly, we change the model space in which the Monte Carlo random walk is performed: one with deeper Moho (crystalline crust thickness is constrained between 58 and 68 km) and the other one with shallower Moho (crust thickness is constrained between 43 and 53 km). Shown in Figures 14b and 14c, these inversions result in different uppermost mantle structures: the deeper Moho case introduces a HVL right beneath the Moho, while the shallower Moho case does not contain a lid. However, the posterior distributions of the average velocity in between 60- and 100-km depth only show minor differences. The average value of the posterior distribution change from 4.44 to 4.46 km/s for the deep Moho case (Figure 14e) and 4.41 km/s for the shallowest Moho case (Figure 14f). For comparison, the average value is 4.60 km/s for point 2 off the GSM (blue distributions in Figure 14). The standard deviation of the posterior distributions is ~ 0.05 km/s (~1%), but the mean value of the average velocity in the uppermost mantle depth is stable with respect to Moho depth variations. These tests enable us to conclude that the GSM anomaly presented in Figure 8 is reliable. Additionally, no evidence shows that such anomaly is due to radial anisotropy.

Fast velocities observed at depths of 120–250 km beneath the GSM strongly indicate that the *craton-style* cold temperatures prevail at these depths. A hypothesis of high-temperature mantle underlain by a low-temperature lithospheric root is thus difficult to support and is inconsistent with the GSM being generally considered to be an Archean/Proterozoic block with no significant tectonism since the Mesozoic (Ferraccioli et al., 2011; Hansen et al., 2010; Heeszel et al., 2013). Any temperature perturbation in the lithosphere from earlier, deeper mantle convection should be largely homogenized over this long time period.

Compositional factors, on the other hand, are good candidates to interpret the GSM anomaly. Fertile mantle (with a lower Mg and higher Fe contents, and is capable of producing basaltic melt) has slower seismic velocity than normal subcratonic lithospheric mantle. A decrease of five in the Mg number (or corresponding increase in Fe number) will cause an ~2% decrease of Vs at mantle depths (Deschamps et al., 2002; Godey et al., 2004; Jordan, 1979; Priestley & McKenzie, 2006; Schutt & Lesher, 2006; Yan et al., 1989). A difficulty for such an interpretation is that xenolith studies in other cratonic areas generally reveal a fertile mantle at greater depths. For example, beneath the North America, fertile xenoliths usually originate from about 200-km depth (Gaul et al., 2000; Griffin et al., 1999, 2004; O'Reilly & Griffin, 2006), unless the uppermost mantle has been refertilized. Stealth metasomatic refertilization processes have been proposed (Malkovets et al., 2007; O'Reilly & Griffin, 2013) to generate fertile lherzolite at shallower depths through a continued input of melts/fluids from the asthenosphere below. In our images, the GSM anomaly beneath the GSM does not connect to any vertical slow Vs conduits at greater depths. If such conduits exist, then they are too thin to be observed by our current images.

Another possible mechanism is mantle eclogitization from subduction prior to or during a compressional orogeny that thickened the crust of the GSM. During a continental collision or crustal subduction, partial eclogitization in the uppermost mantle may occur as crustal materials were pushed at mantle depths, and an eclogite-rich (more precisely, granulite-garnet-pyroxenite-rich) zone would form from the foundering of the lower crust (Lee, 2014) or crustal subduction of the colliding plates (Austrheim, 1991). In that case, an uppermost mantle pyroxenite-rich eclogitization zone may be the cause, as pyroxenite has substancially slower velocity than mantle peridotite (Gao et al., 2000). Alternatively, amphibole-rich lithological composition (e.g., restite created by melt extraction at the top of the lithospheric mantle or paragasite
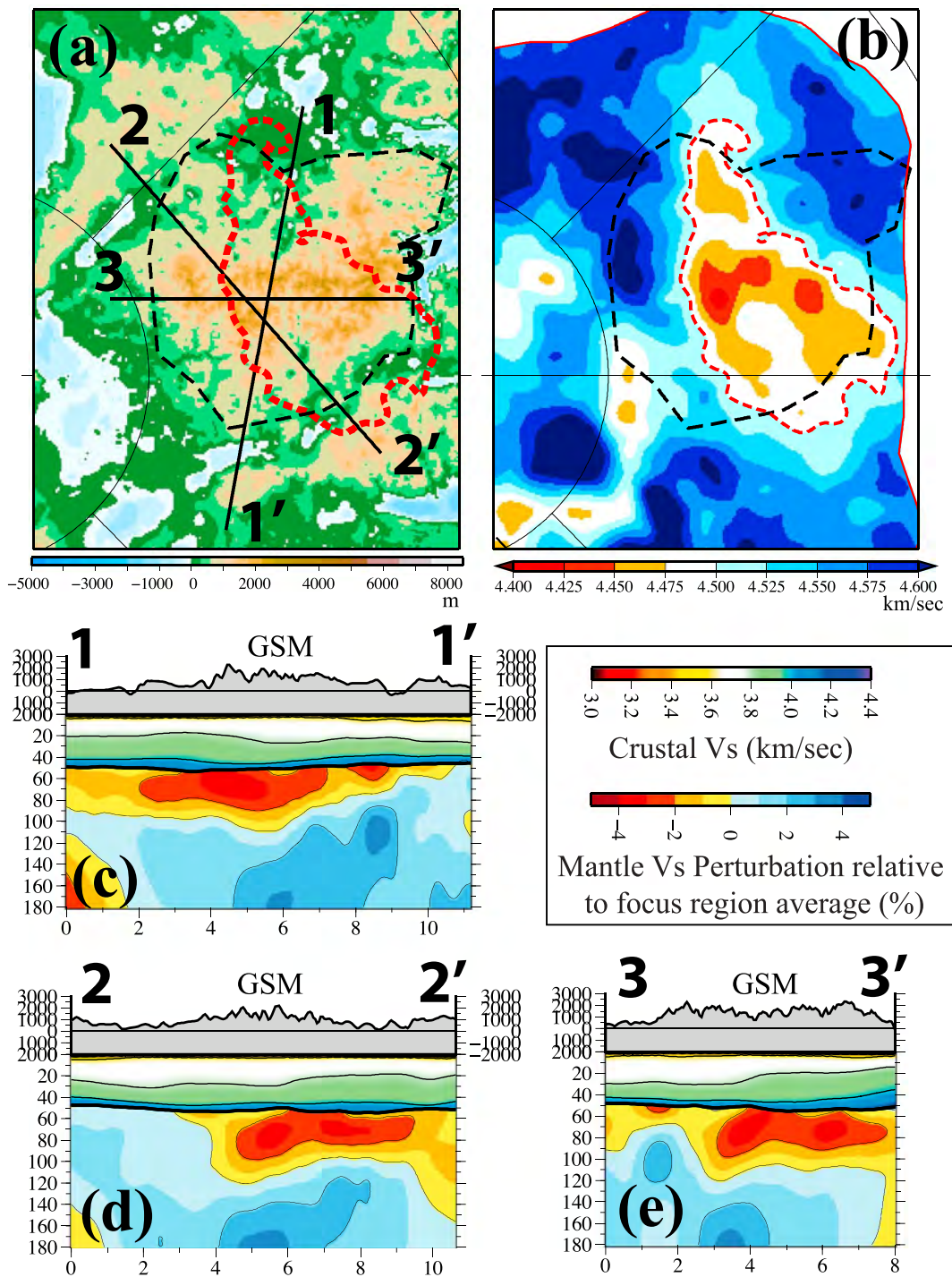
Figure 13. Uppermost mantle slow Vs anomaly beneath the Gamburtsev Subglacial Mountains (GSM). (a) Focus region of the GSM with the subice elevation color coded. The black dashed line marks the region of elevated topography near the GSM. The red dashed line marks the location of the slow uppermost mantle Vs (<4.5 km/s). Locations of vertical transects of 1–1′, 2–2′, and 3–3′ are presented by three straight lines. A small black rectangle marks the location where the reliability of the 1-D Vs model is tested in Figure 14. (b) Vs of the uppermost 50 km of mantle for the focus region. (c-d) Vertical transects along 1–1′, 2–2′, and 3–3′, respectively. Crustal Vs is drawn according to absolute values and mantle Vs is plotted as percentage perturbation relative to the average Vs profile of the focus region.
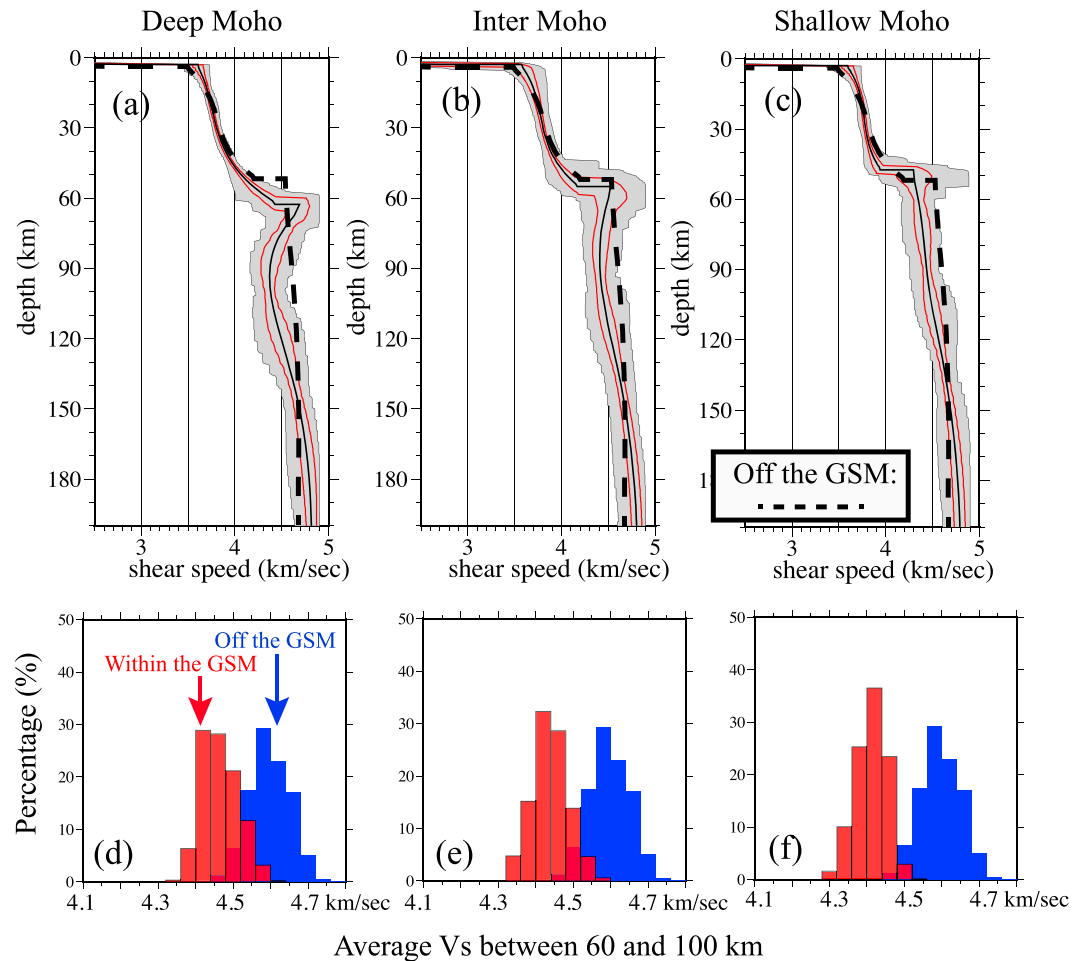
Figure 14. Reliability of the low-velocity anomaly in the uppermost mantle beneath the GSM regarding the uncertainties in the Moho. (a) Resulting 1-D model ensemble (grey corridor) and the average model (black profile) with 1 SD of the posterior distribution (red profiles) for a GSM location (marked in Figure 14a) from a Monte Carlo search with shallow Moho prior constraints. For comparison, the average Vs profile for a point in the EANT but off the GSM is shown as black dashed profile. (b and c) Similar to (a) but from Monte Carlo inversion with intermediate and deep Moho prior constraints, respectively. (d) Posterior marginal distributions for Vs between 60 and 100 km beneath the GSM location (red histogram) and beneath an off-GSM location (blue histogram). (e and f) Similar to (d) but the GSM location's posterior distributions are computed with deeper and shallower Moho prior values, respectively.

usually observed in lherzolite) also has a lower seismic velocity signature. The restite-rich model has been proposed to explain an uppermost mantle LVZ beneath the Baltic Shield (Bruneton et al., 2004). In that study, a combination of 60% of restite and 40% of harzburgite would produce a slower uppermost mantle (~3% slower than the harzburgite mantle xenoliths). In contrast, the paragasite-rich model has been proposed to interpret a moderately slow uppermost mantle in central Australia (Fishwick et al., 2005; Fishwick & Reading, 2008), where the Australian cratons amalgamated/collided in the Proterozoic (Kennett et al., 2012). Notably, the central Australian anomaly displays a similar Vs value at 75-km depth, underlain by very fast anomalies from 125 to 250 km (Fishwick & Reading, 2008). The region is too far away from the GSM to represent the same terrain or to have an identical geological history but probably represent similar phenomena.

Mantle eclogitization and/or the existence of amphibole-rich restites/paragasites preserved in the uppermost mantle would have a substantially different chemical composition compared with normal subcontinental lithospheric mantle rocks. Notably, mantle eclogitization indicates extra density gain from the uppermost mantle, which might resolve the differences of Moho depth seen by seismologic inversion (Hansen et al., 2010; Ramirez et al., 2016) and gravity studies (Block et al., 2009). Since the region has high topography

and a complicated tectonic history (Ferraccioli et al., 2011), other geological and petrological evidences will be required to clarify what mechanism(s) are responsible. Given the high correlation between the localities of the high elevation of the GSM and the upper mantle LVZ, however, if any mechanism explains the LVZ, it will also shed lights on the geomorphic and topographic evolution of the GSM. To better understand this mechanism, a more sophisticated gravity modeling (Fischer, 2002) or joint analysis of seismic evidence and gravity data could usefully test the hypothesis.

7. Summary and Final Comments

We have analyzed a comprehensive collection of seismic data collected from Antarctica to construct the Rayleigh wave phase and group velocity maps using ambient noise cross-correlation. The coherency between the phase velocity maps from ambient noise and from teleseismic earthquakes confirms the high quality of both maps and allows us to combine both data sets to construct local dispersion curves over a wide range of periods (from 8 to ~150 s). Using these local dispersion curves together with P receiver functions, we constructed a 3-D model of the crust and uppermost mantle beneath West and central Antarctica. The model reveals a variety of crustal/uppermost features including (1) a localized uppermost mantle slow velocity belt extending from the Terror Rift in the Ross Sea along the TAM front, and continuing along the front of the EM-WM. This low-velocity zone is likely the trace of a Cenozoic rift system; (2) a mantle delamination with seismic signatures of (a) the missing lithosphere lid beneath the southern TAM, (b) a wedge shaped LVZ beneath the TAM front, and (c) a dipping interface between slow/warm WANT and fast/cold EANT (noted and described in detail in Shen et al., 2018); (3) a region of thin crust and intermediate velocity upper mantle between the EM-WM and PM, a transitional region between the WARS and EANT; (4) thin crust and slow uppermost mantle beneath the ASE, indicating a thin lithosphere in this area; and (5) a slow uppermost mantle beneath the GSM extending to ~100 km depth, which we hypothesize may be a compositional variability related to orogenic processes.

This 3-D model can serve as a basis for future improvements of our understanding of the Antarctic continent. First, the current model does not cover large parts of EANT, as station coverage is still poor in many regions. As more data become available, future extension of the 3-D model to cover the whole continent will be important to reveal additional features. Second, this 3-D model only represents our knowledge of the Vsv structure, to which the Rayleigh waves are most sensitive. Love wave analysis can provide complementary Vsh information and, along with mantle shear wave splitting, allows mapping of the azimuthal and radial anisotropy, which provides important constraints on mantle fabric, deformation history, and flow. Third, by adding other types of measurements such as Rayleigh wave horizontal-to-vertical (H/V) ratios observed with both earthquakes and ambient noise, which is sensitive to the shallowest several km of the Earth (Shen & Ritzwoller, 2016), the ice sheet structure (including its thickness and internal structure) and subice contact can be better constrained. Finally, the data sets collected here can be further exploited by performing thermodynamic inversion to better estimate the thermal structure of Antarctica (e.g., Shapiro & Ritzwoller, 2004). Such a model can provide important estimates of lithospheric thickness, surface heat flow to the base of the ice sheet, and with the incorporation of rheological constraints, mantle viscosity.

References

Accardo, N. J., Wiens, D. A., Hernandez, S., Aster, R. C., Nyblade, A., Huerta, A., et al. (2014). Upper mantle seismic anisotropy beneath the West Antarctic Rift System and surrounding region from shear wave splitting analysis. *Geophysical Journal International*, *198*(1), 414–429. https://doi.org/10.1093/gji/ggu117

An, M., Wiens, D. A., Zhao, Y., Feng, M., Nyblade, A. A., Kanao, M., et al. (2015). S-velocity model and inferred Moho topography beneath the Antarctic Plate from Rayleigh waves. *Journal of Geophysical Research: Solid Earth*, *120*, 359–383. https://doi.org/10.1002/2014JB011332

Aster, R. C., Borchers, B., & Thurber, C. H. (2011). *Parameter estimation and inverse problems* (Vol. 90). Academic Press.

Bannister, S., Snieder, R. K., & Passier, M. L. (2000). Shear-wave velocities under the Transantarctic Mountains and Terror Rift from surface wave inversion. *Geophysical Research Letters*, *27*(2), 281–284. https://doi.org/10.1029/1999GL010866

Barklage, M., Wiens, D. A., Nyblade, A., & Anandakrishnan, S. (2009). Upper mantle seismic anisotropy of South Victoria Land and the Ross Sea coast, Antarctica from SKS and SKKS splitting analysis. *Geophysical Journal International*, *178*(2), 729–741. https://doi.org/10.1111/j.1365-246X.2009.04158.x

Barletta, V. R., Bevis, M., Smith, B. E., Wilson, T., Brown, A., Bordoni, A., et al. (2017). Observed rapid bedrock uplift in Amundsen Sea Embayment promotes ice-sheet stability. *Science*, *360*(6395), 1335–1339.

Barmin, M. P., Ritzwoller, M. H., & Levshin, A. L. (2001). A fast and reliable method for surface wave tomography. In *Monitoring the comprehensive nuclear-test-ban treaty: Surface waves* (pp. 1351–1375). Basel: Birkhäuser.

Behrendt, J. C., & Cooper, A. (1991). Evidence of rapid Cenozoic uplift of the shoulder escarpment of the Cenozoic West Antarctic rift system and a speculation on possible climate forcing. *Geology*, *19*(4), 315–319. https://doi.org/10.1130/0091-7613(1991)019<0315:EORCUO>2.3.CO;2

Behrendt, J. C., LeMasurier, W. E., Cooper, A. K., Tessensohn, F., Trehu, A., & Damaske, D. (1991). Geophysical studies of the West Antarctic rift system. *Tectonics*, *10*(6), 1257–1273.

Bensen, G. D., Ritzwoller, M. H., Barmin, M. P., Levshin, A. L., Lin, F., Moschetti, M. P., et al. (2007). Processing seismic ambient noise data to obtain reliable broad-band surface wave dispersion measurements. *Geophysical Journal International*, *169*(3), 1239–1260. https://doi.org/10.1111/j.1365-246X.2007.03374.x

Bialas, R. W., Buck, W. R., Studinger, M., & Fitzgerald, P. G. (2007). Plateau collapse model for the Transantarctic Mountains–West Antarctic Rift System: Insights from numerical experiments. *Geology*, *35*(8), 687–690. https://doi.org/10.1130/G23825A.1

Blankenship, D. D., Bell, R. E., Hodge, S. M., Brozena, J. M., Behrendt, J. C., & Finn, C. A. (1993). Active volcanism beneath the West Antarctic Ice Sheet and implications for ice-sheet stability. *Nature*, *361*, 526–529.

Block, A. E., Bell, R. E., & Studinger, M. (2009). Antarctic crustal thickness from satellite gravity: Implications for the Transantarctic and Gamburtsev Subglacial Mountains. *Earth and Planetary Science Letters*, *288*(1-2), 194–203. https://doi.org/10.1016/j.epsl.2009.09.022

Bodin, T., Sambridge, M., Tkalčić, H., Arroucau, P., Gallagher, K., & Rawlinson, N. (2012). Transdimensional inversion of receiver functions and surface wave dispersion. *Journal of Geophysical Research*, *117*, B02301. https://doi.org/10.1029/2011JB008560

Boger, S. D. (2011). Antarctica—Before and after Gondwana. *Gondwana Research*, *19*(2), 335–371. https://doi.org/10.1016/j.gr.2010.09.003

Brenn, G. R., Hansen, S. E., & Park, Y. (2017). Variable thermal loading and flexural uplift along the Transantarctic Mountains, Antarctica. *Geology*, *45*(5), 463–466. https://doi.org/10.1130/G38784.1

Bromirski, P. D., Chen, Z., Stephen, R. A., Gerstoft, P., Arcas, D., Diez, A., et al. (2017). Tsunami and infragravity waves impacting Antarctic ice shelves. *Journal of Geophysical Research: Oceans*, *122*, 5786–5801. https://doi.org/10.1002/2017JC012913

Bromirski, P. D., Diez, A., Gerstoft, P., Stephen, R. A., Bolmer, T., Wiens, D. A., et al. (2015). Ross Ice Shelf vibrations. *Geophysical Research Letters*, *42*, 7589–7597. https://doi.org/10.1002/2015GL065284

Bruneton, M., Pedersen, H. A., Farra, V., Arndt, N. T., Vacher, P., Achauer, U., et al. (2004). Complex lithospheric structure under the central Baltic Shield from surface wave tomography. *Journal of Geophysical Research*, *109*, B10303. https://doi.org/10.1029/2003JB002947

Cande, S. C., Stock, J. M., Müller, R. D., & Ishihara, T. (2000). Cenozoic motion between east and West Antarctica. *Nature*, *404*(6774), 145–150. https://doi.org/10.1038/35004501

Chaput, J., Aster, R. C., Huerta, A., Sun, X., Lloyd, A., Wiens, D., et al. (2014). The crustal thickness of West Antarctica. *Journal of Geophysical Research: Solid Earth*, *119*, 378–395. https://doi.org/10.1002/2013JB010642

Dalton, C. A., Ekström, G., & Dziewoński, A. M. (2008). The global attenuation structure of the upper mantle. *Journal of Geophysical Research*, *113*, B09303. https://doi.org/10.1029/2007JB005429

Dalziel, I. W. D. (2007). The Ellsworth Mountains: Critical and Enduringly Enigmatic. In A. K. Cooper, et al. (Eds.), *Antarctica: A Keystone in a Changing World – Online Proceedings of the 10th ISAES, USGS Open-File Report 2007-1047, Short Research Paper 004* (5 p.). https://doi.org/10.3133/of2007-1047.srp004

Danesi, S., & Morelli, A. (2000). Group velocity of Rayleigh waves in the Antarctic region. *Physics of the Earth and Planetary Interiors*, *122*(1-2), 55–66. https://doi.org/10.1016/S0031-9201(00)00186-2

Danesi, S., & Morelli, A. (2001). Structure of the upper mantle under the Antarctic plate from surface wave tomography. *Geophysical Research Letters*, *28*(23), 4395–4398. https://doi.org/10.1029/2001GL013431

Deng, Y., Shen, W., Xu, T., & Ritzwoller, M. H. (2015). Crustal layering in northeastern Tibet: A case study based on joint inversion of receiver functions and surface wave dispersion. *Geophysical Journal International*, *203*(1), 692–706. https://doi.org/10.1093/gji/ggv321

Deschamps, F., Trampert, J., & Snieder, R. (2002). Anomalies of temperature and iron in the uppermost mantle inferred from gravity data and tomographic models. *Physics of the Earth and Planetary Interiors*, *129*(3-4), 245–264. https://doi.org/10.1016/S0031-9201(01)00294-1

Diez, A., Bromirski, P. D., Gerstoft, P., Stephen, R. A., Anthony, R. E., Aster, R. C., et al. (2016). Ice shelf structure derived from dispersion curve analysis of ambient seismic noise, Ross Ice Shelf, Antarctica. *Geophysical Journal International*, *205*(2), 785–795. https://doi.org/10.1093/gji/ggw036

Du Toit, A. L. (1937). *Our wandering continents: An hypothesis of continental drifting*. Oliver and Boyd.

Emry, E. L., Nyblade, A. A., Julià, J., Anandakrishnan, S., Aster, R. C., Wiens, D. A., et al. (2015). The mantle transition zone beneath West Antarctica: Seismic evidence for hydration and thermal upwellings. *Geochemistry, Geophysics, Geosystems*, *16*, 40–58. https://doi.org/10.1002/2014GC005588

Fahnestock, M., Abdalati, W., Joughin, I., Brozena, J., & Gogineni, P. (2001). High geothermal heat flow, basal melt, and the origin of rapid ice flow in central Greenland. *Science*, *294*(5550), 2338–2342. https://doi.org/10.1126/science.1065370

Faul, U., & Jackson, I. (2015). Transient creep and strain energy dissipation: An experimental perspective. *Annual Review of Earth and Planetary Sciences*, *43*, 541–569.

Ferraccioli, F., Armadillo, E., Jordan, T., Bozzo, E., & Corr, H. (2009). Aeromagnetic exploration over the East Antarctic Ice Sheet: A new view of the Wilkes Subglacial Basin. *Tectonophysics*, *478*(1–2), 62–77. https://doi.org/10.1016/j.tecto.2009.03.013

Ferraccioli, F., Finn, C. A., Jordan, T. A., Bell, R. E., Anderson, L. M., & Damaske, D. (2011). East Antarctic rifting triggers uplift of the Gamburtsev Mountains. *Nature*, *479*(7373), 388–392. https://doi.org/10.1038/nature10566

Finotello, M., Nyblade, A., Julia, J., Wiens, D., & Anandakrishnan, S. (2011). Crustal Vp-Vs ratios and thickness for Ross Island and the Transantarctic Mountain front, Antarctica. *Geophysical Journal International*, *185*(1), 85–92. https://doi.org/10.1111/j.1365-246X.2011.04946.x

Fischer, K. M. (2002). Waning buoyancy in the crustal roots of old mountains. *Nature*, *417*(6892), 933–936. https://doi.org/10.1038/nature00855

Fishwick, S., Kennett, B. L. N., & Reading, A. M. (2005). Contrasts in lithospheric structure within the Australian craton—Insights from surface wave tomography. *Earth and Planetary Science Letters*, *231*(3-4), 163–176. https://doi.org/10.1016/j.epsl.2005.01.009

Fishwick, S., & Reading, A. M. (2008). Anomalous lithosphere beneath the Proterozoic of western and central Australia: A record of continental collision and intraplate deformation? *Precambrian Research*, *166*(1-4), 111–121. https://doi.org/10.1016/j.precamres.2007.04.026

Fitzsimons, I. C. W. (2000a). A review of tectonic events in the East Antarctic Shield and their implications for Gondwana and earlier super-continents. *Journal of African Earth Sciences*, *31*(1), 3–23. https://doi.org/10.1016/S0899-5362(00)00069-5

Fitzsimons, I. C. W. (2000b). Grenville-age basement provinces in East Antarctica: Evidence for three separate collisional orogens. *Geology*, *28*(10), 879–882. https://doi.org/10.1130/0091-7613(2000)28<879:GBPIEA>2.0.CO;2

Forsyth, D. W., & Li, A. (2005). Array analysis of two-dimensional variations in surface wave phase velocity and azimuthal anisotropy in the presence of multipathing interference. *Seismic Earth: Array Analysis of Broadband Seismograms*, *157*, 81–97.

Fretwell, P., Pritchard, H. D., Vaughan, D. G., Bamber, J. L., Barrand, N. E., Bell, R., et al. (2013). Bedmap2: Improved ice bed, surface and thickness datasets for Antarctica. *The Cryosphere*, *7*(1), 375–393. https://doi.org/10.5194/tc-7-375-2013

Gao, S., Kern, H., Liu, Y. S., Jin, S. Y., Popp, T., Jin, Z. M., et al. (2000). Measured and calculated seismic velocities and densities for granulites from xenolith occurrences and adjacent exposed lower crustal sections: A comparative study from the North China craton. *Journal of Geophysical Research: Solid Earth*, *105*(B8), 18,965–18,976.

Gaul, O. F., Griffin, W. L., O'Reilly, S. Y., & Pearson, N. J. (2000). Mapping olivine composition in the lithospheric mantle. *Earth and Planetary Science Letters*, *182*(3-4), 223–235. https://doi.org/10.1016/S0012-821X(00)00243-0

Godey, S., Deschamps, F., Trampert, J., & Snieder, R. (2004). Thermal and compositional anomalies beneath the North American continent. *Journal of Geophysical Research*, *109*, B01308. https://doi.org/10.1029/2002JB002263

Gomez, N., Pollard, D., & Holland, D. (2015). Sea-level feedback lowers projections of future Antarctic ice sheet mass loss. *Nature Communications*, *6*(1), 8798. https://doi.org/10.1038/ncomms9798

Granot, R., Cande, S. C., Stock, J. M., Davey, F. J., & Clayton, R. W. (2010). Postspreading rifting in the Adare Basin, Antarctica: Regional tectonic consequences. *Geochemistry, Geophysics, Geosystems*, *11*, Q08005. https://doi.org/10.1029/2010GC003105

Graw, J. H., Adams, A. N., Hansen, S. E., Wiens, D. A., Hackworth, L., & Park, Y. (2016). Upper mantle shear wave velocity structure beneath northern Victoria Land, Antarctica: Volcanism and uplift in the northern Transantarctic Mountains. *Earth and Planetary Science Letters*, *449*, 48–60. https://doi.org/10.1016/j.epsl.2016.05.026

Graw, J. H., & Hansen, S. E. (2017). Upper mantle seismic anisotropy beneath the Northern Transantarctic Mountains, Antarctica from PKS, SKS, and SKKS splitting analysis. *Geochemistry, Geophysics, Geosystems*, *18*(2), 544–557. https://doi.org/10.1002/2016GC006729

Griffin, W. L., O'Reilly, S. Y., Doyle, B. J., Pearson, N. J., Coopersmith, H., Kivi, K., et al. (2004). Lithosphere mapping beneath the North American plate. *Lithos*, *77*(1-4), 873–922. https://doi.org/10.1016/j.lithos.2004.03.034

Griffin, W. L., O'Reilly, S. Y., & Ryan, C. G. (1999). The composition and origin of sub-continental lithospheric mantle. In *Mantle petrology: Field observations and high-pressure experimentation: A tribute to Francis R.(Joe) Boyd* (Vol. 6, pp. 13–45). Houston: The Geochemical Society.

Grunow, A. M., Kent, D. V., & Dalziel, I. W. D. (1991). New paleomagnetic data from Thurston Island: Implications for the tectonincs of West Antarctica and Weddell Sea Opening. *Journal of Geophysical Research*, *96*(B11), 17,935–17,954. https://doi.org/10.1029/91JB01507

Hansen, S. E., Graw, J. H., Kenyon, L. M., Nyblade, A. A., Wiens, D. A., Aster, R. C., et al. (2014). Imaging the Antarctic mantle using adaptively parameterized P-wave tomography: Evidence for heterogeneous structure beneath West Antarctica. *Earth and Planetary Science Letters*, *408*, 66–78. https://doi.org/10.1016/j.epsl.2014.09.043

Hansen, S. E., Julia, J., Nyblade, A. A., Pyle, M. L., Wiens, D. A., & Anandakrishnan, S. (2009). Using S wave receiver functions to estimate crustal structure beneath ice sheets: An application to the Transantarctic Mountains and East Antarctic craton. *Geochemistry, Geophysics, Geosystems*, *10*, Q08014. https://doi.org/10.1029/2009GC002576

Hansen, S. E., Kenyon, L. M., Graw, J. H., Park, Y., & Nyblade, A. A. (2016). Crustal structure beneath the northern Transantarctic Mountains and Wilkes subglacial basin: Implications for tectonic origins. *Journal of Geophysical Research: Solid Earth*, *121*, 812–825. https://doi.org/10.1002/2015JB012325

Hansen, S. E., Nyblade, A. A., Heeszel, D. S., Wiens, D. A., Shore, P., & Kanao, M. (2010). Crustal structure of the Gamburtsev Mountains, East Antarctica, from S-wave receiver functions and Rayleigh wave phase velocities. *Earth and Planetary Science Letters*, *300*(3-4), 395–401. https://doi.org/10.1016/j.epsl.2010.10.022

Hansen, S. E., Reusch, A. M., Parker, T., Bloomquist, D. K., Carpenter, P., Graw, J. H., & Brenn, G. R. (2015). The Transantarctic Mountains Northern Network (TAMNNET): Deployment and performance of a seismic array in Antarctica. *Seismological Research Letters*, *86*(6), 1636–1644. https://doi.org/10.1785/0220150117

Heeszel, D. S., Wiens, D. A., Anandakrishnan, S., Aster, R. C., Dalziel, I. W., Huerta, A. D., et al. (2016). Upper mantle structure of central and West Antarctica from array analysis of Rayleigh wave phase velocities. *Journal of Geophysical Research: Solid Earth*, *121*, 1758–1775. https://doi.org/10.1002/2015JB012616

Heeszel, D. S., Wiens, D. A., Nyblade, A. A., Hansen, S. E., Kanao, M., An, M., & Zhao, Y. (2013). Rayleigh wave constraints on the structure and tectonic history of the Gamburtsev Subglacial Mountains, East Antarctica. *Journal of Geophysical Research: Solid Earth*, *118*, 2138–2153. https://doi.org/10.1002/jgrb.50171

Ikami, A., & Ito, K. (1986). Crustal structure in the Mizuho Plateau, East Antarctica, by a two-dimensional ray approximation. *Journal of Geodynamics*, *6*(1–4), 271–283. https://doi.org/10.1016/0264-3707(86)90044-X

Jordan, T. A., Ferraccioli, F., Ross, N., Corr, H. F., Leat, P. T., Bingham, R. G., et al. (2013). Inland extent of the Weddell Sea rift imaged by new aerogeophysical data. *Tectonophysics*, *585*, 137–160. https://doi.org/10.1016/j.tecto.2012.09.010

Jordan, T. H. (1979). Mineralogies, densities and seismic velocities of garnet lherzolites and their geophysical implications. In *The Mantle Sample: Inclusion in Kimberlites and Other Volcanics* (pp. 1–14). https://doi.org/10.1029/SP016p0001

Joughin, I., Smith, B. E., & Medley, B. (2014). Marine ice sheet collapse potentially underway for the Thwaites Glacier Basin, West Antarctica. *Science*, *344*(6185), 735–738. https://doi.org/10.1126/science.1249055

Kang, D., Shen, W., Ning, J., & Ritzwoller, M. H. (2016). Seismic evidence for lithospheric modification associated with intracontinental volcanism in northeastern China. *Geophysical Journal International*, *204*(1), 215–235. https://doi.org/10.1093/gji/ggv441

Kennett, B. L., Fichtner, A., Fishwick, S., & Yoshizawa, K. (2012). Australian seismological reference model (AuSREM): Mantle component. *Geophysical Journal International*, *192*(2), 871–887.

Kennett, B. L. N., Engdahl, E. R., & Buland, R. (1995). Constraints on seismic velocities in the Earth from traveltimes. *Geophysical Journal International*, *122*(1), 108–124. https://doi.org/10.1111/j.1365-246X.1995.tb03540.x

King, M. A., Bingham, R. J., Moore, P., Whitehouse, P. L., Bentley, M. J., & Milne, G. A. (2012). Lower satellite-gravimetry estimates of Antarctic sea-level contribution. *Nature*, *491*(7425), 586–589. https://doi.org/10.1038/nature11621

Kogan, A. L. (1972). Results of deep seismic soundings of the Earth's crust in East Antarctica. *Antarctic Geology and Geophysics*, 485–489.

Larter, R. D., Anderson, J. B., Graham, A. G., Gohl, K., Hillenbrand, C. D., Jakobsson, M., et al. (2014). Reconstruction of changes in the Amundsen Sea and Bellingshausen Sea sector of the West Antarctic Ice Sheet since the last glacial maximum. *Quaternary Science Reviews*, *100*, 55–86. https://doi.org/10.1016/j.quascirev.2013.10.016

Lawrence, J. F., Wiens, D. A., Nyblade, A. A., Anandakrishnan, S., Shore, P. J., & Voigt, D. (2006a). Rayleigh wave phase velocity analysis of the Ross Sea, Transantarctic Mountains, and East Antarctica from a temporary seismograph array. *Journal of Geophysical Research*, *111*, B06302. https://doi.org/10.1029/2005JB003812

Lawrence, J. F., Wiens, D. A., Nyblade, A. A., Anandakrishan, S., Shore, P. J., & Voigt, D. (2006b). Upper mantle thermal variations beneath the Transantarctic Mountains inferred from teleseismic S-wave attenuation. *Geophysical Research Letters*, *33*, L03303. https://doi.org/10.1029/2005GL024516

Lawrence, J. F., Wiens, D. A., Nyblade, A. A., Anandakrishnan, S., Shore, P. J., & Voigt, D. (2006c). Crust and upper mantle structure of the Transantarctic Mountains and surrounding regions from receiver functions, surface waves, and gravity: Implications for uplift models. *Geochemistry, Geophysics, Geosystems*, *7*, Q10011. https://doi.org/10.1029/2006GC001282

Lee, C.-T. A. (2014). The physics and chemistry of recycling lower continental crust. In *Treatise of Geochemistry* (2nd ed., vol. 4, pp. 423–456). Elsevier. https://doi.org/10.1016/B978-0-08-095975-7.00314-4

LeMasurier, W. E. (1990). *Late Cenozoic volcanism on the Antarctic Plate: An overview* (pp. 1–17). Washington, DC: American Geophysical Union.

Levshin, A., Pisarenko, V. F., & Pogrebinsky, G. A. (1972). On a frequency-time analysis of oscillations. *Annales de Geophysique*, *28*, 211–218.

Licht, K. J., Groth, T., Townsend, J. P., Hennessy, A. J., Hemming, S. R., Flood, T. P., & Studinger, M. (2018). Evidence for extending anomalous Miocene volcanism at the edge of the East Antarctic craton. *Geophysical Research Letters*, *45*, 3009–3016. https://doi.org/10.1002/2018GL077237

Ligorría, J. P., & Ammon, C. J. (1999). Iterative deconvolution and receiver-function estimation. *Bulletin of the Seismological Society of America*, *89*(5), 1395–1400.

Lin, F. C., & Ritzwoller, M. H. (2011). Apparent anisotropy in inhomogeneous isotropic media. *Geophysical Journal International*, *186*(3), 1205–1219. https://doi.org/10.1111/j.1365-246X.2011.05100.x

Lindeque, A., Gohl, K., Wobbe, F., & Uenzelmann-Neben, G. (2016). Preglacial to glacial sediment thickness grids for the Southern Pacific Margin of West Antarctica. *Geochemistry, Geophysics, Geosystems*, *17*, 4276–4285. https://doi.org/10.1002/2016GC006401

Lloyd, A. J., Nyblade, A. A., Wiens, D. A., Hansen, S. E., Kanao, M., Shore, P. J., & Zhao, D. (2013). Upper mantle seismic structure beneath central East Antarctica from body wave tomography: Implications for the origin of the Gamburtsev Subglacial Mountains. *Geochemistry, Geophysics, Geosystems*, *14*, 902–920. https://doi.org/10.1002/ggge.20098

Lloyd, A. J., Wiens, D., Zhu, H., Tromp, J., Nyblade, A., Anandakrishnan, S., et al. (2017). Full waveform adjoint seismic tomography of the Antarctic Plate. In 2017 Fall Meeting.

Lloyd, A. J., Wiens, D. A., Nyblade, A. A., Anandakrishnan, S., Aster, R. C., Huerta, A. D., et al. (2015). A seismic transect across West Antarctica: Evidence for mantle thermal anomalies beneath the Bentley Subglacial Trench and the Marie Byrd Land Dome. *Journal of Geophysical Research: Solid Earth*, *120*, 8439–8460. https://doi.org/10.1002/2015JB012455

Lough, A. C., Wiens, D. A., Barcheck, C. G., Anandakrishnan, S., Aster, R. C., Blankenship, D. D., et al. (2013). Seismic detection of an active subglacial magmatic complex in Marie Byrd Land, Antarctica. *Nature Geoscience*, *6*(12), 1031–1035. https://doi.org/10.1038/ngeo1992

Malkovets, V. G., Griffin, W. L., O'Reilly, S. Y., & Wood, B. J. (2007). Diamond, subcalcic garnet, and mantle metasomatism: Kimberlite sampling patterns define the link. *Geology*, *35*(4), 339–342. https://doi.org/10.1130/G23092A.1

Merdith, A. S., Collins, A. S., Williams, S. E., Pisarevsky, S., Foden, J. D., Archibald, D. B., et al. (2017). A full-plate global reconstruction of the Neoproterozoic. *Gondwana Research*, *50*, 84–134. https://doi.org/10.1016/j.gr.2017.04.001

Morelli, A., & Danesi, S. (2004). Seismological imaging of the Antarctic continental lithosphere: A review. *Global and Planetary Change*, *42*(1-4), 155–165. https://doi.org/10.1016/j.gloplacha.2003.12.005

Moschetti, M. P., Ritzwoller, M. H., Lin, F. C., & Yang, Y. (2010). Crustal shear wave velocity structure of the western United States inferred from ambient seismic noise and earthquake data. *Journal of Geophysical Research*, *115*, B10306. https://doi.org/10.1029/2010JB007448

Mosegaard, K., & Tarantola, A. (1995). Monte Carlo sampling of solutions to inverse problems. *Journal of Geophysical Research*, *100*(B7), 12,431–12,447. https://doi.org/10.1029/94JB03097

O'Donnell, J. P., & Nyblade, A. A. (2014). Antarctica's hypsometry and crustal thickness: Implications for the origin of anomalous topography in East Antarctica. *Earth and Planetary Science Letters*, *388*, 143–155. https://doi.org/10.1016/j.epsl.2013.11.051

O'Donnell, J. P., Selway, K., Nyblade, A. A., Brazier, R. A., Wiens, D. A., Anandakrishnan, S., et al. (2017). The uppermost mantle seismic velocity and viscosity structure of central West Antarctica. *Earth and Planetary Science Letters*, *472*, 38–49. https://doi.org/10.1016/j.epsl.2017.05.016

O'Reilly, S. Y., & Griffin, W. L. (2006). Imaging global chemical and thermal heterogeneity in the subcontinental lithospheric mantle with garnets and xenoliths: Geophysical implications. *Tectonophysics*, *416*(1-4), 289–309. https://doi.org/10.1016/j.tecto.2005.11.014

O'Reilly, S. Y., & Griffin, W. L. (2013). Mantle metasomatism. In *Metasomatism and the chemical transformation of rock* (pp. 471–533). Berlin, Heidelberg: Springer.

Panter, K. S., Kyle, P. R., & Smellie, J. L. (1997). Petrogenesis of a phonolite–trachyte succession at Mount Sidley, Marie Byrd Land, Antarctica. *Journal of Petrology*, *38*(9), 1225–1253. https://doi.org/10.1093/petroj/38.9.1225

Phillips, E. H., Sims, K. W., Blichert-Toft, J., Aster, R. C., Gaetani, G. A., Kyle, P. R., et al. (2018). The nature and evolution of mantle upwelling at Ross Island, Antarctica, with implications for the source of HIMU lavas. *Earth and Planetary Science Letters*, *498*, 38–53.

Pollard, D., DeConto, R. M., & Nyblade, A. A. (2005). Sensitivity of Cenozoic Antarctic ice sheet variations to geothermal heat flux. *Global and Planetary Change*, *49*(1–2), 63–74. https://doi.org/10.1016/j.gloplacha.2005.05.003

Priestley, K., & McKenzie, D. (2006). The thermal structure of the lithosphere from shear wave velocities. *Earth and Planetary Science Letters*, *244*(1-2), 285–301. https://doi.org/10.1016/j.epsl.2006.01.008

Pyle, M. L., Wiens, D. A., Nyblade, A. A., & Anandakrishnan, S. (2010). Crustal structure of the Transantarctic Mountains near the Ross Sea from ambient seismic noise tomography. *Journal of Geophysical Research*, *115*, B11310. https://doi.org/10.1029/2009JB007081

Ramirez, C., Nyblade, A., Emry, E. L., Julià, J., Sun, X., Anandakrishnan, S., et al. (2017). Crustal structure of the Transantarctic Mountains, Ellsworth Mountains and Marie Byrd Land, Antarctica: Constraints on shear wave velocities, Poisson's ratios and Moho depths. *Geophysical Journal International*, *211*(3), 1328–1340. https://doi.org/10.1093/gji/ggx333

Ramirez, C., Nyblade, A., Hansen, S. E., Wiens, D. A., Anandakrishnan, S., Aster, R. C., et al. (2016). Crustal and upper-mantle structure beneath ice-covered regions in Antarctica from S-wave receiver functions and implications for heat flow. *Geophysical Journal International*, *204*(3), 1636–1648. https://doi.org/10.1093/gji/ggv542

Ritzwoller, M. H., Lin, F. C., & Shen, W. (2011). Ambient noise tomography with a large seismic array. *Comptes Rendus Geoscience*, *343*(8-9), 558–570. https://doi.org/10.1016/j.crte.2011.03.007

Ritzwoller, M. H., Shapiro, N. M., Levshin, A. L., & Leahy, G. M. (2001). Crustal and upper mantle structure beneath Antarctica and surrounding oceans. *Journal of Geophysical Research*, *106*(B12), 30,645–30,670. https://doi.org/10.1029/2001JB000179

Robinson, E. S., & Splettstoesser, J. F. (1984). *Structure of the Transantarctic Mountains determined from geophysical surveys* (pp. 119–162). Washington, DC: American Geophysical Union.

Rocchi, S., Storti, F., Di Vincenzo, G., & Rossetti, F. (2003). Intraplate strike-slip tectonics as an alternative to mantle plume activity for the Cenozoic rift magmatism in the Ross Sea region, Antarctica. *Geological Society, London, Special Publications*, *210*(1), 145–158. https://doi.org/10.1144/GSL.SP.2003.210.01.09

Rouland, D., & Roult, G. (1992). Phase velocity distribution beneath Antarctica and surrounding oceans. In Y. Yoshida, et al. (Eds.), *Recent progress in Antarctic Science* (pp. 483–487).

Sabra, K. G., Gerstoft, P., Roux, P., Kuperman, W. A., & Fehler, M. C. (2005). Extracting time-domain Green's function estimates from ambient seismic noise. *Geophysical Research Letters*, *32*, L03310. https://doi.org/10.1029/2004GL021862

Salvini, F., Brancolini, G., Busetti, M., Storti, F., Mazzarini, F., & Coren, F. (1997). Cenozoic geodynamics of the Ross Sea region, Antarctica: Crustal extension, intraplate strike-slip faulting, and tectonic inheritance. *Journal of Geophysical Research*, *102*(B11), 24,669–24,696. https://doi.org/10.1029/97JB01643

Schutt, D. L., & Lesher, C. E. (2006). Effects of melt depletion on the density and seismic velocity of garnet and spinel lherzolite. *Journal of Geophysical Research*, *111*, B05401. https://doi.org/10.1029/2003JB002950

Seroussi, H., Ivins, E. R., Wiens, D. A., & Bondzio, J. (2017). Influence of a West Antarctic mantle plume on ice sheet basal conditions. *Journal of Geophysical Research: Solid Earth*, *122*, 7127–7155. https://doi.org/10.1002/2017JB014423

Shapiro, N. M., Campillo, M., Stehly, L., & Ritzwoller, M. H. (2005). High-resolution surface-wave tomography from ambient seismic noise. *Science*, *307*(5715), 1615–1618. https://doi.org/10.1126/science.1108339

Shapiro, N. M., & Ritzwoller, M. H. (2002). Monte-Carlo inversion for a global shear-velocity model of the crust and upper mantle. *Geophysical Journal International*, *151*(1), 88–105. https://doi.org/10.1046/j.1365-246X.2002.01742.x

Shapiro, N. M., & Ritzwoller, M. H. (2004). Inferring surface heat flux distributions guided by a global seismic model: Particular application to Antarctica. *Earth and Planetary Science Letters*, *223*(1-2), 213–224. https://doi.org/10.1016/j.epsl.2004.04.011

Shen, W., & Ritzwoller, M. H. (2016). Crustal and uppermost mantle structure beneath the United States. *Journal of Geophysical Research: Solid Earth*, *121*, 4306–4342. https://doi.org/10.1002/2016JB012887

Shen, W., Ritzwoller, M. H., Kang, D., Kim, Y., Lin, F. C., Ning, J., et al. (2016). A seismic reference model for the crust and uppermost mantle beneath China from surface wave dispersion. *Geophysical Journal International*, *206*(2), 954–979. https://doi.org/10.1093/gji/ggw175

Shen, W., Ritzwoller, M. H., & Schulte-Pelkum, V. (2013). A 3-D model of the crust and uppermost mantle beneath the Central and Western US by joint inversion of receiver functions and surface wave dispersion. *Journal of Geophysical Research: Solid Earth*, *118*, 262–276. https://doi.org/10.1029/2012JB009602

Shen, W., Ritzwoller, M. H., Schulte-Pelkum, V., & Lin, F. C. (2013). Joint inversion of surface wave dispersion and receiver functions: A Bayesian Monte-Carlo approach. *Geophysical Journal International*, *192*(2), 807–836.

Shen, W., Wiens, D. A., Stern, T., Anandakrishnan, S., Aster, R. C., Dalziel, I., et al. (2018). Seismic evidence for lithospheric foundering beneath the southern Transantarctic Mountains, Antarctica. *Geology*, *46*(1), 71–74. https://doi.org/10.1130/G39555.1

Siddoway, C. S. (2008). Tectonics of the West Antarctic Rift System: New light on the history and dynamics (pembroke, ont.) of distributed intracontinental extension. *Antarctica: A Keystone in a Changing World*, 91–114.

Sieminski, A., Debayle, E., & Lévêque, J. J. (2003). Seismic evidence for deep low-velocity anomalies in the transition zone beneath West Antarctica. *Earth and Planetary Science Letters*, *216*(4), 645–661. https://doi.org/10.1016/S0012-821X(03)00518-1

Stern, T. A., & ten Brink, U. S. (1989). Flexural uplift of the Transantarctic Mountains. *Journal of Geophysical Research*, *94*(B8), 10,315–10,330. https://doi.org/10.1029/JB094iB08p10315

Studinger, M., Bell, R. E., Buck, W. R., Karner, G. D., & Blankenship, D. D. (2004). Sub-ice geology inland of the Transantarctic Mountains in light of new aerogeophysical data. *Earth and Planetary Science Letters*, *220*(3–4), 391–408. https://doi.org/10.1016/S0012-821X(04)00066-4

Stump, E., Sheridan, M. F., Borg, S. G., & Sutter, J. F. (1980). Early Miocene subglacial basalts, the East Antarctic ice sheet, and uplift of the Transantarctic Mountains. *Science*, *207*(4432), 757–759. https://doi.org/10.1126/science.207.4432.757

ten Brink, U. S., Bannister, S., Beaudoin, B. C., & Stern, T. A. (1993). Geophysical investigations of the tectonic boundary between east and West Antarctica. *Science*, *261*(5117), 45–50. https://doi.org/10.1126/science.261.5117.45

ten Brink, U. S., Hackney, R. I., Bannister, S., Stern, T. A., & Makovsky, Y. (1997). Uplift of the Transantarctic Mountains and the bedrock beneath the East Antarctic ice sheet. *Journal of Geophysical Research*, *102*(B12), 27,603–27,621. https://doi.org/10.1029/97JB02483

Trabant, C., Hutko, A. R., Bahavar, M., Karstens, R., Ahern, T., & Aster, R. (2012). Data products at the IRIS DMC: Stepping stones for research and other applications. *Seismological Research Letters*, *83*(5), 846–854.

van der Wal, W., Whitehouse, P. L., & Schrama, E. J. (2015). Effect of GIA models with 3D composite mantle viscosity on GRACE mass balance estimates for Antarctica. *Earth and Planetary Science Letters*, *414*, 134–143.

Veevers, J. J. (2012). Reconstructions before rifting and drifting reveal the geological connections between Antarctica and its conjugates in Gondwanaland. *Earth-Science Reviews*, *111*(3-4), 249–318. https://doi.org/10.1016/j.earscirev.2011.11.009

Vuan, A., Maurice, S. R., Wiens, D. A., & Panza, G. F. (2005). Crustal and upper mantle S-wave velocity structure beneath the Bransfield Strait (West Antarctica) from regional surface wave tomography. *Tectonophysics*, *397*(3-4), 241–259. https://doi.org/10.1016/j.tecto.2004.12.011

Wannamaker, P., Hill, G., Stodt, J., Maris, V., Ogawa, Y., Selway, K., et al. (2017). Uplift of the central transantarctic mountains. *Nature Communications*, *8*(1), 1588. https://doi.org/10.1038/s41467-017-01577-2

Watson, T., Nyblade, A., Wiens, D. A., Anandakrishnan, S., Benoit, M., Shore, P. J., et al. (2006). P and S velocity structure of the upper mantle beneath the Transantarctic Mountains, East Antarctic craton, and Ross Sea from travel time tomography. *Geochemistry, Geophysics, Geosystems*, *7*(7), Q07005. https://doi.org/10.1029/2005GC001238

Weaver, S. D., Storey, B. C., Pankhurst, R. J., Mukasa, S. B., DiVenere, V. J., & Bradshaw, J. D. (1994). Antarctica-New Zealand rifting and Marie Byrd Land lithospheric magmatism linked to ridge subduction and mantle plume activity. *Geology*, *22*(9), 811–814. https://doi.org/10.1130/0091-7613(1994)022<0811:ANZRAM>2.3.CO;2

Wessel, P., & Smith, W. H. (1998). New, improved version of Generic Mapping Tools released. *Eos, Transactions American Geophysical Union*, *79*(47), 579–579.

Wörner, G. (1999). Lithospheric dynamics and mantle sources of alkaline magmatism of the Cenozoic West Antarctic Rift System. *Global and Planetary Change*, *23*(1-4), 61–77. https://doi.org/10.1016/S0921-8181(99)00051-X

Yan, B., Graham, E. K., & Furlong, K. P. (1989). Lateral variations in upper mantle thermal structure inferred from three-dimensional seismic inversion models. *Geophysical Research Letters*, *16*(5), 449–452. https://doi.org/10.1029/GL016i005p00449

Yang, Y., & Forsyth, D. W. (2006). Regional tomographic inversion of the amplitude and phase of Rayleigh waves with 2-D sensitivity kernels. *Geophysical Journal International*, *166*(3), 1148–1160. https://doi.org/10.1111/j.1365-246X.2006.02972.x